J. Fluid Mech. (2008), *vol.* 613, *pp.* 135–169.
doi:10.1017/S0022112008003017 Printed in the United Kingdom

Numerical simulations of boundary-layer bypass transition due to high-amplitude free-stream turbulence

VICTOR OVCHINNIKOV[1], MEELAN M. CHOUDHARI[2] AND UGO PIOMELLI[3]†

[1]Department of Chemical Engineering, Massachusetts Institute of Technology, Cambridge, MA 02139 USA

[2]NASA Langley Research Center, Hampton, VA 23681, USA

[3]Department of Mechanical Engineering, University of Maryland, College Park, MD 20742, USA

(Received 4 April 2007 and in revised form 13 June 2008)

Direct numerical simulations (DNS) of bypass transition due to high-amplitude free-stream turbulence (FST) are carried out for a flat-plate boundary layer. The computational domain begins upstream of the plate leading edge and extends into the fully turbulent region. Thus, there is no *ad hoc* treatment to account for the initial ingestion of FST into the laminar boundary layer. We study the effects of both the FST length scale and the disturbance behaviour near the plate leading edge on the details of bypass transition farther downstream. In one set of simulations, the FST parameters are chosen to match the ERCOFTAC benchmark case T3B. The inferred FST integral length scale L_{11} is significantly larger ($R_L = UL_{11}/\nu = 6580$) than that employed in previous simulations of bypass transition ($R_L \simeq 1000$). An additional set of simulations was performed at $R_L = 1081$ to compare the transition behaviour in the T3B case with that of a smaller value of FST length scale. The FST length scale is found to have a profound impact on the mechanism of transition. While streamwise streaks (Klebanoff modes) are observed at both values of the FST length scale, they appear to have clear dynamical significance only at the smaller value of R_L, where transition is concomitant with streak breakdown. For the T3B case, turbulent spots form upstream of the region where streaks could be detected. Spot precursors are traced to quasi-periodic spanwise structures, first observed as short wavepackets in the wall-normal velocity component inside the boundary layer. These structures are reoriented to become horseshoe vortices, which break down into young turbulent spots. Two of the four spots examined for this case had a downstream-pointing shape, similar to those found in experimental studies of transitional boundary layers. Additionally, our simulations indicate the importance of leading-edge receptivity for the onset of transition. Specifically, higher fluctuations of the vertical velocity at the leading edge of the plate result in higher levels of streamwise Reynolds stress inside the developing boundary layer, facilitating breakdown to turbulence.

† Present address: Department of Mechanical and Materials Engineering, Queen's University, Kingston, ON, CANADA, K7L 3N6

1. Introduction

In many wall-bounded flows of engineering interest, it is desirable to control the onset of laminar–turbulent transition. In aerospace applications, it may be advantageous to maintain laminar flow over a major portion of an airfoil to reduce drag. In low-pressure turbines, the state of the boundary layer flow has an impact on its ability to negotiate adverse pressure gradients and, hence, influences the energy efficiency of the turbine device. Transition to turbulence has therefore been the focus of extensive research in the past century.

Traditionally, the study of transition in a boundary layer has been approached from the point of view of linear stability. When the Tollmien–Schlichting (TS) wave amplitude exceeds approximately 1% of the free-stream velocity, the perturbed boundary layer develops secondary three-dimensional instabilities, which harbinger the onset of transition. Because TS waves grow on a viscous time scale, they typically attain the amplitudes required for secondary instability to set in only when the boundary-layer Reynolds number is large, of the order of 10^6.

In many flows with a higher-amplitude disturbance environment, however, transition is observed at Reynolds numbers of the order of 10^5 and does not involve the TS mechanism. The term 'bypass transition' (Morkovin 1969) has been used to describe various cases in which the TS waves are bypassed. The case of boundary-layer bypass transition due to free-stream turbulence (FST) has received recent attention, and is the focus of this study.

1.1. *Experimental work on transition due to FST*

Klebanoff (1971) observed that a Blasius boundary layer subjected to FST develops low-frequency spanwise undulations in the streamwise velocity distribution within the boundary layer. The amplitude of the peak response increased in proportion to the FST amplitude, and grew larger in proportion to the boundary-layer thickness. Kendall (1985) observed long streamwise streaks with small spanwise scales, which he called Klebanoff modes. Matsubara & Alfredsson (2001) have reviewed several experiments performed at the Royal Institute of Technology in Stockholm (KTH). They observe that the spanwise spacing of streaks increases with the FST level, and also slightly increases with the downstream distance. They suggested that the spanwise scale selection occurs within the boundary layer. In a later publication, however, Fransson & Alfredsson (2003) conclude that the selection process is more complex and is influenced by the FST length scale, among other effects.

Fransson, Matsubara & Alfredsson (2005) performed additional experiments using a wide range of FST intensities and length scales and made several important observations. First, there is an initial region near the leading edge where the amplitude of boundary-layer fluctuations grows more slowly than farther downstream, i.e. the transient growth process begins a finite distance downstream from the leading edge. Second, the disturbance energy increases in proportion to both the FST energy and the flat-plate Reynolds number. Third, the transition Reynolds number is inversely proportional to the FST energy. Finally, the extent of the transition zone increases in proportion to the flat-plate Reynolds number. Although Fransson *et al.* (2005) varied the FST length scale in a controlled manner, they did not sort their data based on the length scale. Thus, the effect of the FST length scale is not addressed in their work. Jonáš, Mazur & Uruba (2000) studied the effect of the FST dissipation length scale on the onset of transition at the FST intensity of 3%. Based on their measurements

of the intermittency, they noted that the onset of transition moved upstream with increasing FST length scale, and that the transition region became longer. However, their study did not address the effect of length scale on the details of the transition process and, in particular, whether or not the FST length scale had any effect on the physical mechanism(s) underlying the onset of transition.

1.2. *Computational work*

Large-eddy simulations (LES) and direct numerical simulations (DNS) of transition in boundary layers have been slow to appear, owing to the large computational requirements involved. The first DNS of boundary-layer transition due to FST in a spatial formulation was performed by Rai & Moin (1993), who used a fifth-order upwind biased finite-difference fractional-step compressible Navier–Stokes solver to model the experiments of Blair (1983). The disturbance was generated to match the von Kármán energy spectrum with a prescribed intensity and length scale. The predicted location of transition onset showed reasonable agreement with the experimental data, but the skin friction development farther downstream was compromised because of under-resolution. Their work also indicated that the resolution needed to simulate a transitional flow is at least as high as that for a turbulent boundary layer.

Voke & Yang (1995) used a finite-volume conservative method to perform an LES of boundary-layer transition, in an attempt to reproduce the experiments of Roach & Brierley (1992). Although their simulations were severely under-resolved and the FST properties were not matched to the experiment, they were able to provide qualitative insights into the transition mechanism. The interaction of the wall-normal FST component with the mean shear was proposed to be the key mechanism for the production of Reynolds shear stress, which, together with the mean shear, drives the production of the streamwise Reynolds stress.

A well-resolved DNS of FST-induced transition was performed by Jacobs & Durbin (2001). To provide a somewhat realistic inflow condition without simulating the flow around the leading edge, these authors chose to expand the FST and the associated inflow disturbance profile in terms of the eigenfunctions of the linear Orr–Sommerfeld operator (Grosch & Salwen 1978). With a fine, turbulent-like resolution in the entire boundary layer, they obtained very good agreement with the T3A experiment of Roach & Brierley (1992) at 3% FST intensity. Klebanoff modes were found to be a prominent feature of their simulations, and were generated nonlinearly by the penetration of the FST into the boundary layer. The spanwise streak spacing was in agreement with the optimal results of Andersson *et al.* (1999). No evidence of streak instability was reported in their work. Instead, low-speed streaks provide a receptivity path between the FST and the boundary layer, but are otherwise irrelevant to transition. The onset of transition was attributed to the direct penetration of the free-stream disturbance into the perturbed laminar boundary layer.

Brandt, Schlatter & Henningson (2004) performed DNS of boundary-layer transition due to FST with variable length scale and intensity. They used a similar method to Jacobs & Durbin (2001) to generate the inflow disturbance, but also included the Squire modes for the wall-normal vorticity. They found that for a given FST intensity, increasing the FST length scale moves the onset of transition upstream. The spanwise scale of streaks did not vary appreciably with the FST length scale. Many aspects of their simulations are in qualitative agreement with the experiments of Matsubara & Alfredsson (2001). Using flow visualizations, Brandt *et al.* (2004)

conclude that streak breakdown and turbulent spot formation is caused by either of two types of instability modes of low-speed streaks. The sinuous mode, characterized by streak oscillations in the spanwise direction, was observed more frequently than the varicose mode of instability.

Zaki & Durbin (2005) performed a theoretical and computational analysis of boundary-layer bypass transition within the framework of coupled modes of the linear Orr–Sommerfeld (OS) and Squire operators. The former are sheltered by the boundary-layer mean shear to varying degrees: modes with low frequency and low wall-normal wavenumber are able to 'penetrate' into the boundary layer and excite the corresponding Squire modes, whereas high-frequency modes are not. This fact prompted Zaki & Durbin to define a coupling coefficient to measure the effectiveness of the OS modes in generating low-frequency boundary-layer 'breathing modes' via the excitation of the Squire modes. Using DNS, they show that including a high-frequency (low-penetrating) OS mode at the inflow boundary, in addition to a low-frequency mode, is sufficient to cause transition to turbulence.

Nagarajan, Lele & Ferziger (2007) studied the influence of a blunt superelliptical leading edge on bypass transition by LES. They employed compressible-flow equations at low Mach number. FST was generated to match the von Kármán spectrum, and several values of the FST intensity and length scale were used in the simulations. They found that at low levels of FST and the superellipse aspect ratio $AR = 10$, transition occurs via streak instabilities, similarly to those observed by Brandt *et al.* (2004). At higher levels of the FST intensity and/or length scale, and the leading-edge aspect ratio of $AR = 6$, they observed a different transition mechanism, characterized by localized wavepacket-like oscillations in the spanwise velocity fluctuation, which grew in spatial extent and amplitude as they were convected downstream, and eventually broke down into turbulence. These wavepackets were traced to the stretching of free-stream vortices around the leading edge: particularly strong vortices produce streamwise vortical disturbances in the boundary layer that give rise to the wavepackets. Nagarajan *et al.* showed that the wavepackets have markedly different properties from the spot precursors found in the cases of breakdown due to streak instability.

1.3. *Aim of the current work*

In this study we perform high-resolution DNS of boundary-layer transition due to FST of large amplitude and length scale. The flow around the plate leading edge is explicitly computed within the simulation, and the FST characteristics, including the FST length scale, are matched with the measured data from the T3B experiment of Roach & Brierley (1992).

Our goal is to approximate the T3B experiment with sufficient fidelity that the simulation database can be used to examine the underlying transition physics as well as to guide the development of physics-based engineering prediction methods. Two additional simulations are performed with a smaller FST length scale in order to examine the effects of length scale variation on the transition mechanism. To our knowledge, this is the first numerical study of bypass transition in which the FST length scale is much larger than the transitional boundary-layer thickness. The paper is organized as follows. Section 2 outlines the problem formulation, simulation parameters, and validation. Section 3 describes the results, starting with a statistical examination of the flow fields, moving on to a discussion of the effects of various FST parameters on the transition characteristics, and finishing with a visualization study of the transition process. Section 4 provides a discussion and concluding remarks.

2. Problem formulation

We use the incompressible Navier–Stokes (NS) equations to perform DNS of boundary-layer transition due to FST. The equations of continuity and momentum

$$\frac{\partial u_j}{\partial x_j} = 0, \tag{2.1}$$

$$\frac{\partial u_i}{\partial t} + \frac{\partial}{\partial x_j}(u_j u_i) = -\frac{1}{\rho}\frac{\partial p}{\partial x_i} + \nu \nabla^2 u_i + f_i, \tag{2.2}$$

are discretized using a second-order-accurate finite-difference method on a staggered Cartesian grid. The method fully conserves mass, momentum and kinetic energy in the discrete sense (see Morinishi *et al.* 1998). The presence of the body forces f_i is due to the immersed-boundary method, described at the end of this section. The coordinates x, y, and z refer, respectively, to the streamwise, wall-normal, and spanwise directions. The velocity components in these directions are, respectively, u, v and w. All grids used are uniform in the spanwise direction z, and stretched in the streamwise and wall-normal directions to allow accurate resolution of boundary-layer disturbances, particularly in the transitional region. The equations are integrated in time using an explicit fractional time-step method (Chorin 1968; Kim & Moin 1985), in which the convective and diffusive terms are advanced in time using the second-order-accurate Adams–Bashforth method. The algorithm was parallelized using the message-passing interface (MPI). The code has been previously validated for a variety of turbulent (Balaras, Benocci & Piomelli 1995; Balaras, Piomelli & Wallace 2001), re-laminarizing (Piomelli, Balaras & Pascarelli 2000), and transitional (Ovchinnikov, Piomelli & Choudhari 2006) flows. More details on the implementation can be found in these references.

2.1. *Determination of FST length scale*

The primary goal of the current investigation was to study the mechanism of bypass transition in a realistic high-intensity FST environment. Thus, the configuration of the main simulations was chosen to approximate the wind tunnel experiment T3B by Roach & Brierley (1992), which involved an FST amplitude of 6% of the free-stream velocity at the leading edge.

The available experimental data include the evolution of the FST intensity with the streamwise distance, but not its integral length scale, L_{11}, defined as

$$L_{11} = \int_0^\infty \frac{\overline{u'(x)u'(x+r)}}{\overline{u'(x)u'(x)}}\mathrm{d}r. \tag{2.3}$$

In experimental measurements of homogeneous turbulence that use hot-wire anemometry, L_{11} is approximated from the integral time scale using Taylor's frozen turbulence hypothesis as

$$L_{11} \simeq U_{conv}\int_0^\infty \frac{\overline{u'(t)u'(t+s)}}{\overline{u'(t)u'(t)}}\mathrm{d}s. \tag{2.4}$$

In the above, u' denotes the free-stream velocity fluctuation, U_{conv}, the local mean velocity in the frozen turbulence approximation, and the overbar the long-time average. The energy dissipation length scale, defined as

$$L_k = -\frac{k^{3/2}}{U_\infty \mathrm{d}k/\mathrm{d}x}, \tag{2.5}$$

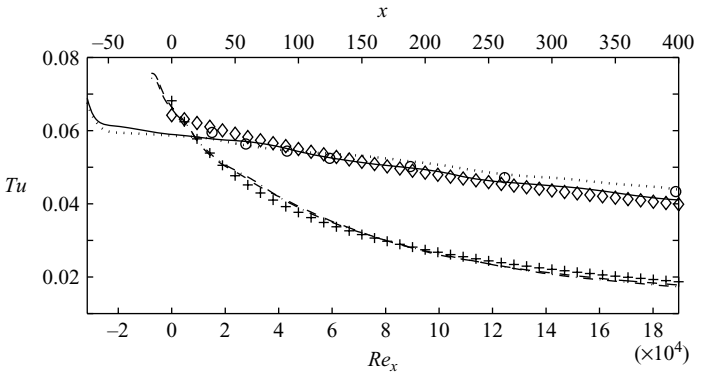

FIGURE 1. Evolution of the FST intensity. ———, Case T3Bs; ·····, Case T3Bf; – – –, Case SLSs; —·—, Case SLSf; ○, T3B experiment of Roach & Brierley (1992); +, Power law $y = C(x - x_0)^{\alpha}$ with $C = 1.4$, $x_0 = -75$, $\alpha = -0.7$; ◇, Power law $y = C(x - x_0)^{\alpha}$ with $C = 3.0$, $x_0 = -370$, $\alpha = -0.65$.

where k denotes the turbulent kinetic energy, can be computed directly from the streamwise FST intensity evolution. According to this definition, the smaller the turbulence decay rate, the larger the associated length scale value, consistent with the conventional spatial understanding of the length scale.

In the following discussion, R denotes the half-thickness of the plate, and is chosen as the length scale for non-dimensional quantities. (This choice of normalization is made here for convenience; we do not assert that R is a physically relevant parameter in transition.) R is also equivalent to the leading-edge radius of the plate in the T3B experiment.

For the T3B experimental data, assuming isotropy of the incoming FST, we found $L_k = 25R$ at the leading edge. To match the measured FST decay in the experiment, we chose $L_{11} = 14R$; this condition also ensures that $L_k = 25R$, as derived from the experimental data. We note that our value for L_{11} is in fair agreement with a recent empirical estimate of $L_{11} = 16.7R$ (Johnson & Ercan 1999), which was based on the data of Roach (1987). Two simulations were carried out with $L_{11} = 14R$. From this point on, we will refer to these as the T3B simulations.

Two additional simulations were performed in this study. The essential difference from the T3B simulations is that the FST integral length scale was set to $2.3R$, which is similar to the values used in other numerical investigations of FST-induced bypass transition. These two simulations will be denoted as cases SLS, in which SLS abbreviates 'small length scale'. The main purpose of the SLS simulations is to compare the transition features in this well-studied regime to the T3B case. The computational details of the four simulations, denoted by T3Bs, T3Bf, SLSs, and SLSf, are described in the next section.

In the simulations of Brandt *et al.* (2004), L_{11} was varied between $1R$ and $3R$, when converted to our units. (The conversion was made by comparing the values of the Reynolds number based on the FST length scale.) This value was specified at $Re^*_{\delta} = 300$ in their simulation and not upstream of the leading edge, as in ours. From the data of Jacobs & Durbin we estimated L_k to be $3.1R$. The leading edge was not included in the computational domain of the simulations discussed in both references. The evolution of the FST intensity for the T3B experiment and our simulations is shown in figure 1. Negative values of x correspond to locations upstream of the

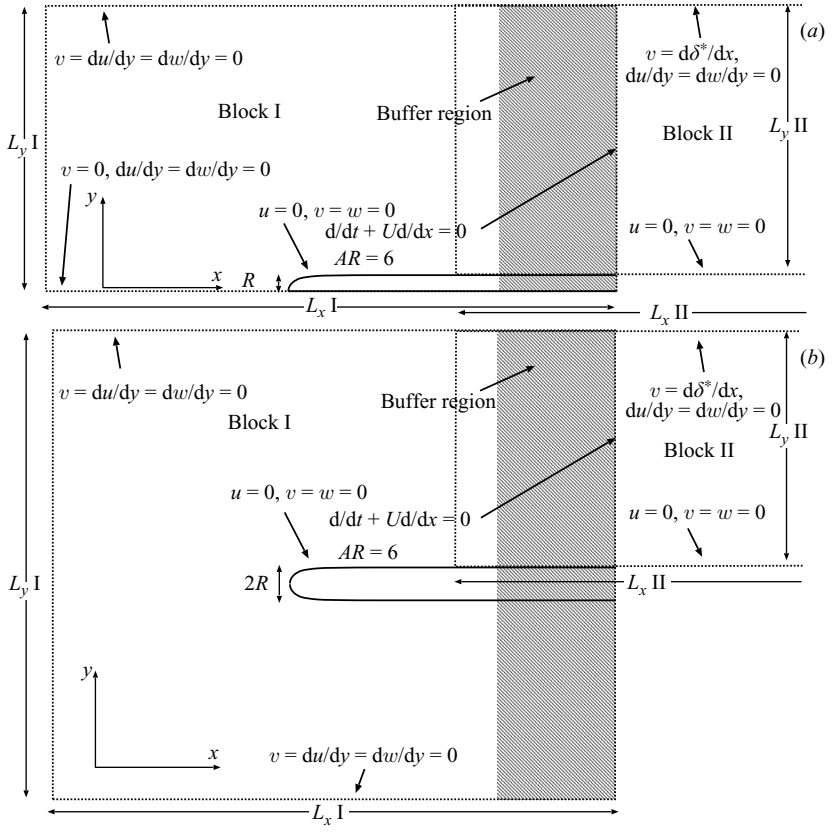

FIGURE 2. Computational configuration and boundary conditions; (*a*) domain with symmetry plane; (*b*) full domain.

leading edge, and the irregular behaviour near the inflow plane is due to the initial adjustment of a synthetic disturbance field. A comparison of the streamwise evolution of the integral length scale with the corresponding power laws is shown in an Appendix available with the online version of the paper, § A.1.

2.2. *Computational domains*

The two types of computational domain used for our simulations are illustrated in figure 2, and simulation parameters are summarized in table 1. Because the T3B simulations presented in this study required substantial computational resources, two approximations were made to decrease the cost of computation.

First, each computational domain was split into two overlapping blocks along the streamwise direction. The first box contained the flat-plate superellipse, and had very fine resolution near the plate leading edge. A short distance downstream, at $x = 15$ and $x = 20$ for the SLS and T3B cases, respectively, a time-sequence of planes of velocity was stored and used as the inflow condition for a second computational domain. This domain had fewer points in the wall-normal direction, but maintained the fine streamwise resolution required to resolve the transition zone. The multi-block approach has been successfully used in the past (Huai, Joslin & Piomelli, 1997). However, strictly speaking, it violates the ellipticity of the incompressible NS equations (the pressure in the two blocks is not mutually coupled). The errors due to multi-block splitting were estimated by Ovchinnikov *et al.* (2006), in the related

Case		L_{11}	Re_L	$L_x \times L_y \times L_z$	$nx \times ny \times nz$	Largest grid size at wall $\Delta x^+ \times \Delta y^+_{wall,max} \times \Delta z^+$
SLSs	Block I	2.3	1081	$38 \times 31 \times 23$	$288 \times 222 \times 192$	$10 \times 0.6 \times 3.5$
	Block II			$538 \times 30 \times 23$	$1472 \times 160 \times 192$	$12 \times 0.7 \times 3.8$
SLSf	Block I	2.3	1081	$38 \times 62 \times 23$	$288 \times 444 \times 192$	$9.5 \times 0.6 \times 3.5$
	Block II			$538 \times 30 \times 23$	$1472 \times 160 \times 192$	$12 \times 0.7 \times 3.6$
T3Bs	Block I	14	6580	$120 \times 67 \times 67$	$504 \times 240 \times 512$	$10 \times 0.8 \times 4.0$
	Block II			$330 \times 66 \times 67$	$882 \times 170 \times 512$	$10 \times 0.8 \times 3.5$
T3Bf	Block I	14	6580	$120 \times 133 \times 67$	$480 \times 421 \times 540$	$10 \times 0.8 \times 3.8$
	Block II			$330 \times 66 \times 67$	$864 \times 170 \times 540$	$10 \times 0.8 \times 3.3$

TABLE 1. Simulation parameters. The FST integral length scale is reported at the leading edge. The FST intensity at the leading edge is 5.9% and 6.7% for cases T3B and SLS, respectively. The location of the inflow boundary of the first simulation box was at $x = -15$ and $x = -65$ relative to the plate leading edge for cases SLS and T3B, respectively. All lengths are shown in the units of the plate half-thickness, R. Re_L is the Reynolds number based on the free-stream velocity, U_∞, and L_{11}.

context of boundary-layer bypass transition due to a cylinder wake, and were found to be insignificant.

Even with the multi-block approach, computing the flow around the entire leading edge turned out to be costly for the T3B case: the calculation would require around 190 million points. This high cost was primarily due to the need for a domain that is large enough to accommodate the FST integral scales, yet resolved finely enough to capture the smallest boundary-layer scales. Thus, to perform a T3B calculation with good statistical convergence, we chose to make the second approximation that the mid-plane of the plate can be represented as a plane of symmetry. The symmetry assumption halves the computational cost in the first block, reducing the overall cost to 140 million points. We will refer to this calculation as the T3Bs case. To have a qualitative indicator of the accuracy of the symmetry approximation, we carried out another simulation using the entire domain, the T3Bf case, but for only one half of the integration time of the T3Bs case. The corresponding statistical sample is not as well converged, and to facilitate comparisons between T3Bs and T3Bf cases, we apply a low-pass filter to the T3Bf data in the streamwise development plots.

To further quantify the errors due to the symmetry approximation, we conducted the SLS simulations with the smaller FST length scale, $L_{11} = 2.3$, both with and without the symmetry condition in the first block. Simulating the SLS case on a full domain is affordable because of the low value for the FST length scale. In the remainder of this paper, SLSs refers to the SLS simulation with the symmetry condition, and SLSf refers to the SLS simulation preformed on the full domain.

2.3. *Leading edge geometry*

The leading edge of the flat plate in the Roach & Brierley (1992) experiment was asymmetrical with a circular tip of radius 0.75 mm. The Reynolds number based on the average free-stream velocity of 9.4 m s^{-1} and the leading-edge radius was 470. In our simulations, we used a symmetrical superellipse with an aspect ratio (AR) of 6.0 to model the leading edge of the plate. The geometry for the superellipse used in our study is given by

$$\left(1 - \frac{1}{AR}\frac{x}{R}\right)^4 + \left(\frac{y}{R}\right)^2 = 1. \tag{2.6}$$

In all of our simulations, the Reynolds number based on the free-stream velocity and the minor half-axis of the superellipse, R, was fixed at 470. The minor axis of the superellipse corresponds to the plate thickness. Note that in order to obtain the Reynolds number based on any length scale expressed in the units of R, one simply multiplies that length scale value by 470. For example, the Reynolds numbers based on the FST length scale for cases T3B and SLS are 6580 and 1081, respectively.

The above geometry was motivated by the availability of two-dimensional numerical data for flow validation, and the assumption that the differences in leading-edge geometry would be less significant when the estimated length scale of the FST is much larger than the leading-edge radius. We note that the symmetry of the leading-edge leads to a suction peak that was probably absent in the reference experiment. However, the experimental configuration cannot be reproduced exactly because the test plate had a flap attached to the end, which cannot be simulated easily. Some discussion of leading-edge-geometry effects measured in wind tunnel experiments can be found in Klingmann *et al.* (1993) and Fransson (2004). Validation of the immersed-boundary representation of the leading edge is described in the next section.

2.4. *Boundary conditions*

The following boundary conditions were applied:

(*a*) The inlet velocities are imposed by adding a zero-mean perturbation field to the uniform mean flow $U=(U_\infty, 0, 0)$. The disturbance was generated using the algorithm due to Rogallo (1981) as described by Jacobs & Durbin (2001), but with Fourier modes, instead of Orr–Sommerfeld modes. The disturbance field has the model spectrum due to von Kármán, and is designed to be homogeneous, isotropic, and divergence-free to avoid large pressure fluctuations near the inflow plane. For all four cases, the FST amplitude in the vicinity of the leading edge was around 6% of U_∞; the three velocity r.m.s. values were within 10% of Tu, which was defined as $(\sqrt{\langle u'u'\rangle}+\sqrt{\langle v'v'\rangle}+\sqrt{\langle w'w'\rangle})/3$. Thus, the FST generated by the Rogallo algorithm is approximately isotropic. The angle brackets denote Reynolds averaging, and the prime a fluctuation from the mean. Further details on the inflow generation can be found in Ovchinnikov, Piomelli & Choudhari (2004).

(*b*) The interface condition between the first and second blocks was obtained by interpolating velocities from the first box onto the wall-normal grid of the second box. The plane from which velocity data were extracted was located at $x=15$ for cases SLSs and SLSf, and $x=20$ for cases T3Bs and T3Bf. The streamwise distances are quoted relative to the leading edge of the plate.

(*c*) At the outlet of each computational block, a convective outflow boundary condition was applied to each velocity component (Orlanski 1976). Simulation results in the last 10–15% of each block were discarded in order to eliminate the effects of proximity to the outflow boundary.

(*d*) In the spanwise direction, z, periodic conditions were used.

(*e*) The no-slip condition was imposed along the plate surface, whereas a symmetry condition was used upstream of the plate leading edge within the first block of cases SLSs and T3Bs.

(*f*) Along the free-stream boundary of the first block of each simulation, we imposed slip-wall conditions, and at the free-stream boundary of the second block, we applied $\partial u/\partial y=0$, $v=\mathrm{d}\delta^*/\mathrm{d}x$, $\partial w/\partial y=0$, where δ^* is the displacement thickness computed for the Blasius velocity profile at each location. The boundary condition on the v-component provides the correct mass flux through the top wall to account for the Blasius boundary-layer growth in the zero-pressure-gradient regime. It becomes

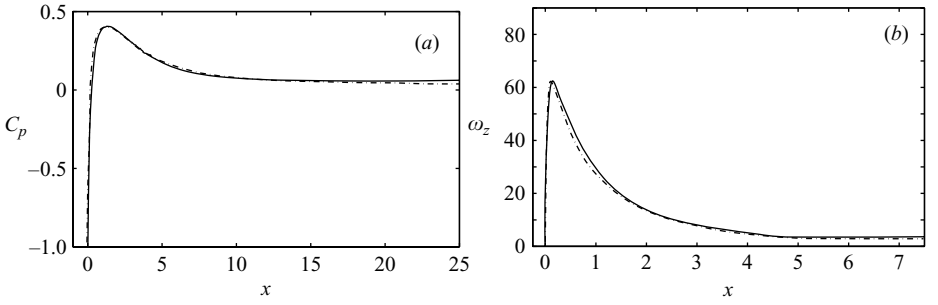

FIGURE 3. Comparison of surface properties for a two-dimensional flow over a superellipse: (*a*) pressure coefficient, C_p; (*b*) wall vorticity, ω_z, ———, current immersed-boundary simulation; —·—, simulation by Lin, Reed & Saric (1992).

less accurate in the transitional and turbulent boundary-layer regions, but does not result in significant free-stream acceleration. In all four simulations, the acceleration coefficient, $K = -(\nu/U_\infty^2)(\mathrm{d}U_\infty/\mathrm{d}x)$ was of the order of 10^{-7} for both blocks. The value of K at which a turbulent boundary layer is expected to re-laminarize is around 3.0×10^{-6} (Spalart 1986). Since the value of K in our case is an order of magnitude lower, we do not expect the acceleration to have an appreciable effect on the onset of transition.

To satisfy the no-slip boundary conditions on the superellipse surface, we employ the immersed-boundary method of Fadlun *et al.* (2000), following the implementation of Balaras (2004). In this procedure, the body forces, f_i, are non-zero only in grid-cells adjacent to the surface, and are assigned in such a way that the velocity on the surface is zero to second-order accuracy. The immersed-boundary method, as described above, has been extensively validated in laminar and turbulent flows. For more details on the implementation, the reader is referred to Fadlun *et al.* (2000) and Balaras (2004).

To ensure that the immersed-boundary representation of the superelliptical leading edge was accurate, we performed a two-dimensional simulation of the flow past a superellipse with $AR = 6$, described by equation (2.6). The computational domain was similar to the one in figure 2(*a*), and extended over 25 and 16 units in the x- and y-directions, respectively, and was resolved with 1075 and 300 cells in the respective directions. The lengths were normalized by the minor half-axis of the superellipse, and the Reynolds number based on this length scale was 2400. This geometry and Reynolds number parameter was chosen to match the calculations of Lin, Reed & Saric (1992), who used an NS solver on a curvilinear grid. Comparisons of the pressure coefficient, $C_p = 2(p - p_\infty)/\rho U_\infty^2$, along the surface of the ellipse, and the vorticity, ω_z, are shown in figure 3. The overall agreement is good. The small discrepancy may be due to the extrapolation of pressure and velocity values from the grid nodes onto the immersed boundary, or the differences in the spatial resolution.

Finally, we note that the immersed-boundary representation of the superellipse was only necessary in the first block of each simulation. The second box was constructed such that its bottom boundary coincides with the surface of the plate.

2.5. *Grid requirements*

The computations performed in this work required long integration times. A typical simulation required a month of clock time on an 8-processor Beowulf cluster (6000 CPU-hours). We were thus unable to perform a grid-refinement study. Ovchinnikov

et al. (2004), however, performed calculations of bypass transition in a configuration similar to the one studied here (their calculations did not include the leading edge and, therefore, were much less demanding computationally). They observe that inadequate streamwise resolution in the transition region may lead to a premature and abrupt transition, probably because energy is aliased into the unstable scales due to under-predicted dissipation. They obtained grid-converged results with the grid spacings, normalized by the friction velocity u_τ and the viscosity ν, of $\Delta x^+ \simeq 7$–12, $\Delta y^+_{wall,max} \simeq 1$ and $\Delta z^+ \simeq 2.5$–3. We used similar values in our calculations, as reported in table 1. Note that these spacings are typical of turbulent flow calculations, and are smaller than those used by Jacobs & Durbin (2001) in their simulations of bypass transition. They used a finite-difference algorithm with second-order spatial accuracy that was similar to the one employed in this study.

To ensure that the computational domains were sufficiently large in the spanwise direction, we computed spanwise correlations of the velocity fluctuations. These will be discussed in detail in § 3.3. For the SLS simulations, in which $L_{11} = 2.3$, the spanwise correlation functions approach the zero line well within the computational domain. For the T3B case, the correlation function is not exactly zero within the domain. However, an additional simulation performed on a domain that was twice as large in the spanwise and wall-normal directions, but without the flat plate, showed that the FST decay rate was unchanged. Therefore, we are confident that the external free-stream environment has been adequately captured.

2.6. *Mean and instantaneous quantities*

In this section, we recall several definitions that will be useful for the remainder of this paper. Mean quantities are defined as

$$F = \langle f(x, y) \rangle = \frac{1}{L_z} \frac{1}{T} \int_0^{L_z} \int_{t-T}^{t} f(x, y, z, \tau)\, \mathrm{d}\tau\, \mathrm{d}z. \tag{2.7}$$

The mean skin friction coefficient

$$C_f = \frac{\tau_w}{\rho U_\infty^2/2} \tag{2.8}$$

is an indicator of transition onset since it increases markedly across the region of laminar–turbulent transition. In this equation, τ_w is the mean wall shear stress, defined as

$$\tau_w = \mu \left\langle \frac{\mathrm{d}u}{\mathrm{d}y} \right\rangle \bigg|_{y=0}. \tag{2.9}$$

The shape factor, H, is defined as $H = \theta/\delta^*$, where δ^* and θ are, respectively, the displacement and momentum thicknesses, given by

$$\delta^* = \int_0^{y_{edge}} \left(1 - \frac{\langle U \rangle}{U_{edge}}\right) \mathrm{d}y; \qquad \theta = \int_0^{y_{edge}} \frac{\langle U \rangle}{U_{edge}} \left(1 - \frac{\langle U \rangle}{U_{edge}}\right) \mathrm{d}y. \tag{2.10}$$

The integration in (2.10) is performed up to the edge of the boundary layer, y_{edge}, taken to be the wall-normal location at which the mean U-velocity gradient falls below 0.01. The effective free-stream velocity, U_{edge}, is the mean velocity at this location. H is also an indicator of transition because the momentum thickness, θ, rises steeply as the flow passes from the laminar to the turbulent regime.

In § 3.4 we will present three-dimensional visualizations of transitional flow fields. To identify vortical structures, we will plot instantaneous isosurfaces of the quantity

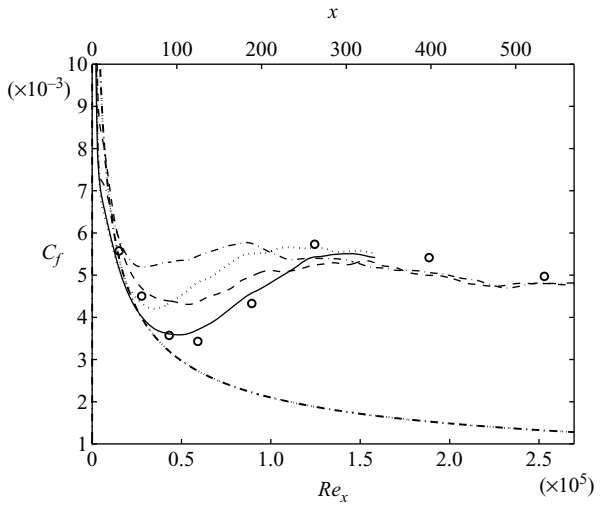

FIGURE 4. Evolution of the skin friction coefficient, C_f. ——, case T3Bs; ·····, case T3Bf; – – –, case SLSs; —·—, case SLSf; ○, T3B experiment of Roach & Brierley (1992); —···—, Blasius C_f. The start of the boundary layer, i.e. the location $x = 0$, is taken to be the tip of the superellipse.

Q defined as

$$Q = -\frac{\partial u_i}{\partial x_j}\frac{\partial u_j}{\partial x_i}. \tag{2.11}$$

2.7. *Statistical convergence*

The governing equations were advanced in time until a statistically stationary state was reached. For cases SLSf, SLSs and T3Bs, flow statistics were subsequently accumulated for a time period required for the mean flow to traverse the entire domain three times. Convergence of the statistical sample in these cases was verified by comparing the statistics based on one half of the time history with those obtained using the entire sample. First-order quantities differed by less than 3%, second moments by less than 6%. For case T3Bf, which was the most computationally intensive, one-and-a-half flow-through periods were recorded. Statistics from this calculation may thus be less reliable.

3. Results

We begin by comparing simulation statistics from cases T3B to the available experimental dataset. Noting discrepancies between cases T3Bs and T3Bf, we examine the effects of the symmetry condition on the transition mechanism and onset location. The discussion reveals the importance of receptivity to fluctuations in the wall-normal velocity at the leading edge of the plate, particularly for cases T3B. We then characterize the transition mechanism for the T3B cases, and demonstrate that it is qualitatively different from that of the SLS cases, which is accompanied by the breakdown of Klebanoff modes.

3.1. *Comparison of T3B simulations with experiment*

The streamwise development of the computed skin friction coefficient, C_f, is shown in figure 4. The approximate locations of transition onset are $x = 100$, $x = 60$, $x = 95$, and $x = 75$ for cases SLSs, SLSf, T3Bs and T3Bf, respectively. The corresponding

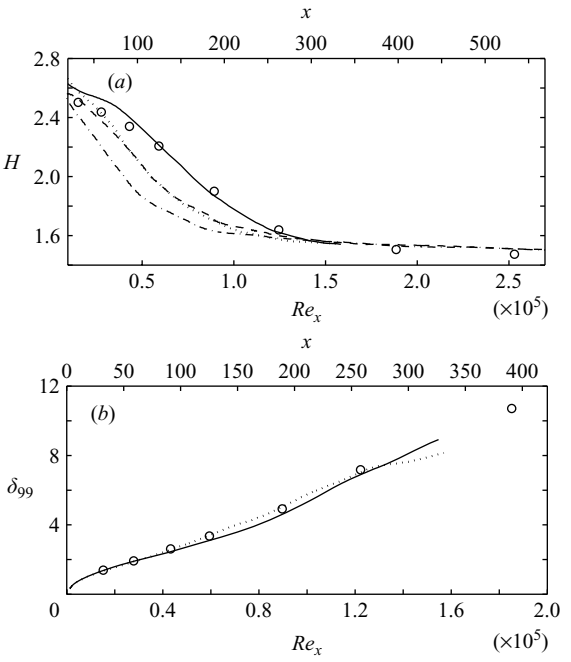

FIGURE 5. Evolution of (*a*) the shape factor, H; (*b*) the boundary-layer thickness, δ_{99} (shown only for cases T3B). ———, case T3Bs; ·····, case T3Bf; – – –, case SLSs; —·—, case SLSf; ○, T3B experiment of Roach & Brierley (1992).

Re_x values are 47 400, 28 440, 45 030, and 35 550. The location of transition onset is nominally defined as the x-location at which the skin friction is at its minimum (young turbulent spots are often observed upstream of this location). The initial mismatch between the Blasius C_f and the simulation data is due to (i) the fact that Blasius similarity is invalid close to the leading edge, (ii) the imposition of the free-slip boundary condition at the top wall of the first block of each simulation, and (iii) the large amplitude of the FST.

The boundary-layer shape factor, H, is shown in figure 5(*a*). H equals 2.6 for Blasius flow and lies around 1.4 for turbulent boundary-layer flow at low values of Re_θ. The shape factor is an inverse measure of the boundary-layer momentum, which increases in the turbulent regime. The differences between the plots in figure 5(*a*) are due to different onsets of transition. Figures 4 and 5(*a*) show that the T3Bs simulation captures the onset and the progress of transition well: $x = 100$ ($Re_x = 47\,000$). However, the onset of transition for case T3Bf occurs significantly farther upstream at $x = 75$ ($Re_x = 35\,550$). This finding is somewhat surprising, since case T3Bf should be a better approximation to the T3B experiment. A detailed examination of the differences between cases T3Bs/f, and also cases SLSs/f, is performed in the next subsection, and reveals the influence of the symmetry condition on the development of boundary-layer Reynolds stress.

Figure 5(*b*) shows the development of the boundary-layer thickness, δ_{99}, for cases T3B. The good agreement between the simulation and experiment indicates that the rate of boundary-layer growth is captured well. The reason the predicted δ_{99} agrees well with the experiment for both T3Bs and T3Bf cases, but only the T3Bs case shows the

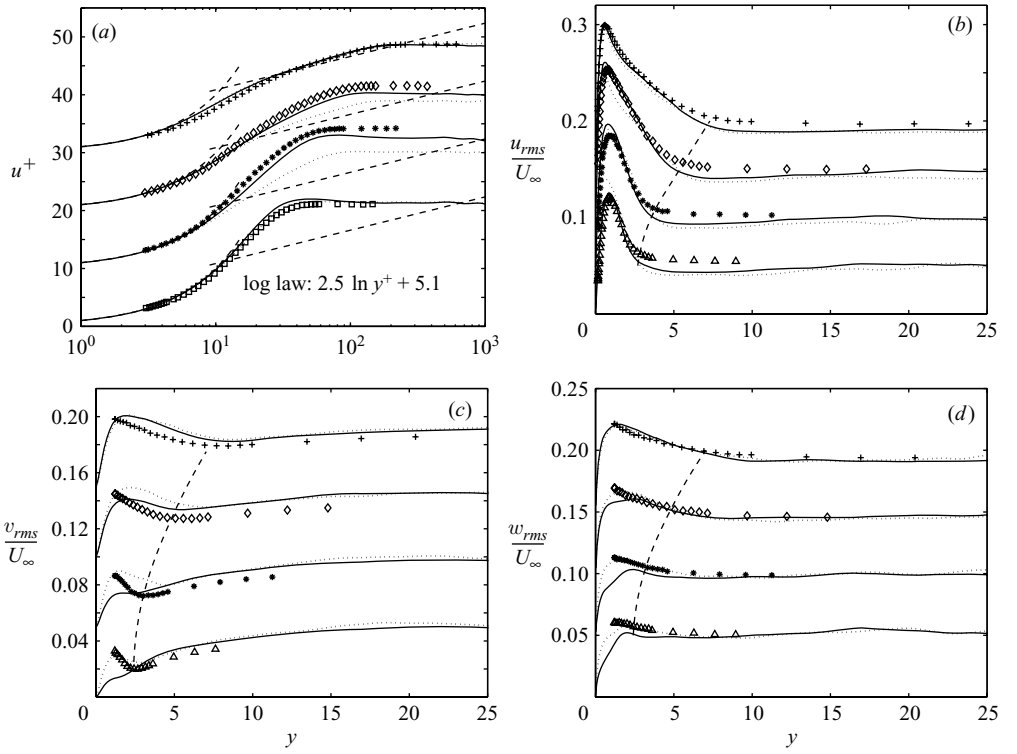

FIGURE 6. Comparison of velocity and turbulent intensities for T3B simulations *vs.* experiment. (*a*) Mean streamwise velocity, u; *b*) u_{rms}; *c*) v_{rms}; *d*) w_{rms}; lines: simulation; ———, T3Bs ·····, T3Bf; symbols: experiment; the dashed line in (*b–d*) marks the location of the boundary-layer edge, δ_{99}; □, $x = 60$, $Re_x = 28\,440$; △, $x = 93$, $Re_x = 44\,082$; ∗, $x = 127$, $Re_x = 60\,198$; ◇, $x = 193$, $Re_x = 91\,482$; +, $x = 260$, $Re_x = 123\,240$; in (*a*) successive curves are shifted in the vertical direction by 10, and in (*b*), (*c*) and (*d*), by 0.05.

correct shape factor evolution, is that the latter depends on the momentum thickness which increases rapidly across transition, which was observed earlier in the T3Bf case.

Further comparison between the T3B simulations and the experiment is shown in figure 6(*a–d*). In figure 6(*a*), velocity profiles corresponding to the T3Bs simulation agree well with the experimental data across the range $x \in [60,\ 260]$, consistent with the agreement in the C_f curve. Figure 6(*b–d*) shows that the evolution of boundary-layer turbulence intensities is also captured well. The dominant component of the boundary-layer perturbation is u' and its profiles agree with the measurements at all four stations shown. The v' and w' profiles in the outer region of the boundary layer also agree well. However, noticeable discrepancies are observed in the near-wall region for the v'-component, particularly at the upstream locations. Fransson & Westin (2002) investigated errors in hot-wire X-probe measurements in the transitional boundary layer by comparing hot-wire and laser Doppler velocimetry (LDV) measurements. A near-wall peak of v_{rms} was present only in the hot-wire dataset, and they concluded that it was an artefact of the hot-wire measurement technique. It can also be seen that the T3Bf v' data give a better match with the experiment. However, judging from the C_f curve in figure 4, at this location the T3Bf dataset corresponds to a later stage in the transition than the experiment, so this agreement is probably coincidental.

The development of the turbulent kinetic energy (TKE) budget across the transitional region is qualitatively similar to that described by Ovchinnikov *et al.* (2006), and is relegated to § A.3 of the online supplement.

Finally, we mention the movement of the stagnation line in simulations T3Bf and SLSf. In both cases, the location of the stagnation point at any spanwise location along the stagnation line was in the range $s \in [-0.1, 0.1]$, where s is the arclength measured from the axis of the leading edge. Time evolution of stagnation point location at a fixed spanwise coordinate showed a quasi-periodic signal with period of approximately 25 in both cases. The length scale of the spanwise variation in the instantaneous stagnation line appears to be proportional to the length scale of the oncoming FST. These observations are summarized in figures 21 and 22 in the online supplement § A.1

3.2. *The effect of symmetry condition: insights into leading-edge receptivity*

Since we observed significant differences in transition onsets between cases T3Bs and T3Bf, in this section we examine the differences between the two simulations. Our focus is on the T3B test case, and important differences from the SLS case will be highlighted at the end of this section.

Cases T3Bs and T3Bf were identical except for the symmetry boundary condition upstream of the leading edge in simulation T3Bs. Even though the FST intensity, shown in figure 1, evolves almost identically for the two cases, the Reynolds stress magnitudes at the boundary-layer edge are different. In figures 7(*a*) and 7(*b*), we compare profiles of the streamwise Reynolds stress $\langle uu \rangle$ and wall-normal Reynolds stress $\langle vv \rangle$, respectively, at several streamwise locations. The short horizontal lines indicate the local boundary-layer thickness, δ_{99}.

In § 3.1 we observed that the location of transition onset is farther downstream in the symmetry-plane case T3Bs. However, figure 7(*a*) shows that for $x \leqslant 20$, the streamwise component of the Reynolds stress at the boundary-layer edge is about twice as high in the T3Bs simulation. The difference in the free-stream TKE between the two cases is diminished by the wall-normal component of the Reynolds stress, which becomes stronger for the T3Bf simulation away from the wall (see figure 7*b* $x =$ 2, 5, 10) so that the turbulence intensities in the free stream are the same, consistent with the streamwise evolution of Tu (cf. figure 1). The spanwise component of the Reynolds stress, $\langle ww \rangle$, is very similar between the two cases and is not shown in figure 7. Although in the T3Bf case, $\langle uu \rangle$ is lower outside, inside the boundary layer it has a sharp peak that is higher in magnitude than that of case T3Bs. The most likely explanation for this behaviour is in the levels of $\langle vv \rangle$ in the vicinity of the flat-plate leading edge.

Exactly at $x = 0$, $\langle vv \rangle$ is approximately six times higher for the T3Bf case than for the T3Bs case. However, at $x = 0$, $\langle vv \rangle$ expressed in Cartesian coordinates corresponds to the component of Reynolds stress tangent to the flat-plate surface. We believe that the $\langle uu \rangle$ peak at locations $x = 2$, 5, 10 for case T3Bf probably arises from the advection of $\langle vv \rangle$ at $x = 0$ along the curvilinear coordinate of the superelliptical surface. In figure 23 in the online supplement § A.2, we compare the components of the Reynolds stress tangent and normal to the flat plate for cases T3B and SLS near the wall. It can be seen that the major effect of the symmetry condition is to remove tangential Reynolds stress in the leading-edge vicinity. The Reynolds stress farther along the surface, which corresponds to $\langle uu \rangle$, is also reduced. These observations suggest that the leading edge couples velocity fluctuations normal to the plate axis at the leading edge to initial levels of the streamwise Reynolds stress in the developing

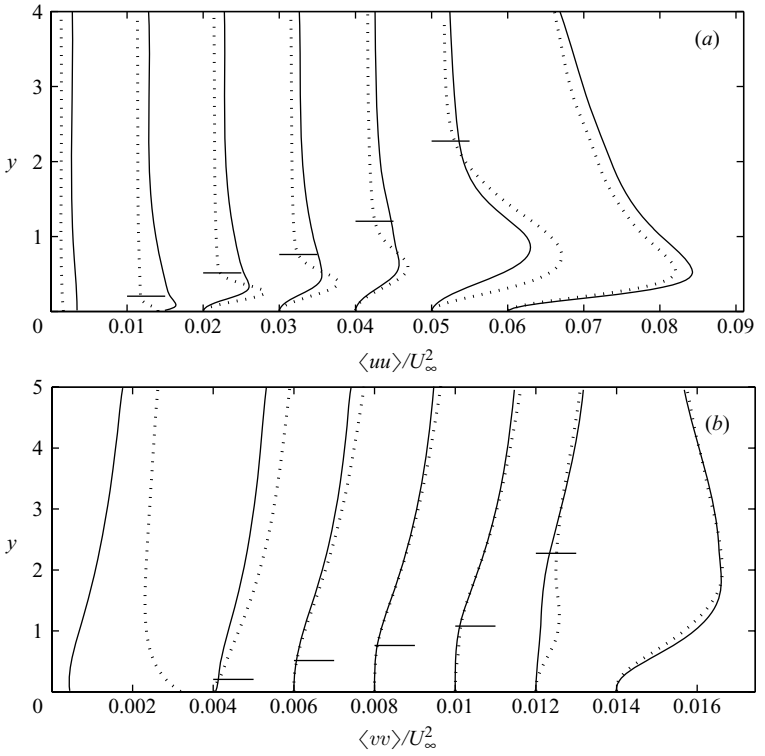

FIGURE 7. Profiles of (*a*) streamwise Reynolds stress $\langle uu \rangle$, and (*b*) the wall-normal Reynolds stress $\langle vv \rangle$. From left to right, the plots correspond to $x = 0$, 2, 5, 10, 20, 75, 250; $Re_x = 0$; 940, 2350, 4700, 9400, 35250, 117500. ——, Case T3Bs; ·····, Case T3Bf; the short horizontal lines indicate the local boundary-layer thickness δ_{99}. On the x-axis, the profiles are offset by 0.01 for (*a*). In (*b*) the first two plots are offset by 0.004 for clarity and the the rest by 0.002.

boundary layer. By employing the symmetry condition, we attenuate this mechanism significantly, thus decreasing the intensity of streamwise velocity perturbation in the downstream boundary layer. We also expect that this receptivity mechanism will be sensitive to the geometry of the leading edge, for example through the effect of leading-edge curvature.

In contrast to its discrepant behaviour at the leading edge, at locations downstream of the leading edge, $\langle vv \rangle$ levels inside the boundary layer are almost the same for the T3B cases with the exception of the boundary-layer $\langle vv \rangle$ peak at $x = 75$. This peak, however, is due to the onset of transition, which is closer upstream for case T3Bf. Voke & Yang (1995) performed a large-eddy simulation of boundary-layer bypass transition and proposed a 'distributed' receptivity mechanism, in which the wall-normal Reynolds stress along the flat surface of the plate drives the production of the Reynolds shear stress. However, the fact that the levels of $\langle vv \rangle$ show little difference between our cases T3Bs/f suggests that such a mechanism does not account for the discrepancies between the two T3B cases. We also note that our observations neither support nor challenge the conclusions of Voke & Yang (1995), but point to an additional mechanism that operates near the leading edge.

The foregoing discussion also suggests possible explanations for the early transition observed for case T3Bf. One possibility is that the wall-normal turbulence intensity i.e. Tv) in the experiment of Roach & Brierley (1992) is significantly lower than Tu.

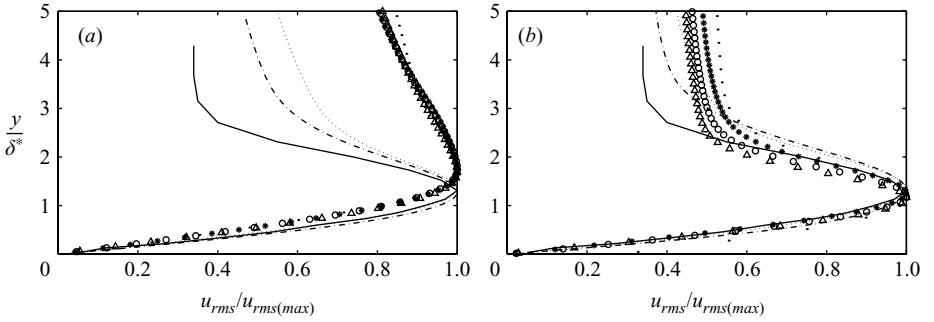

FIGURE 8. Normalized profiles of u_{rms} across the boundary layer; δ^* is the local displacement thickness; (*a*) case T3Bs; (*b*) case T3Bf; ●, $x = 4$; △, $x = 8$; ○, $x = 12$; *, $x = 15$; ·····, $x = 54$; —·—, $x = 73$; ———, self-similar profiles from wind tunnel measurements of Matsubara & Alfredsson (2001).

Another possibility is that in the experiment, the receptivity to $\langle vv \rangle$ at the leading edge is lower because of its different shape. Roach & Brierley (1992) report, however, that the FST generated using their grids was 'extremely isotropic'. The second hypothesis should be investigated in a future study, where the curvature of the leading edge, for example, is varied while FST parameters are kept fixed.

In figure 8(*a*, *b*) we show wall-normal u_{rms} profiles for the two T3B cases, normalized by the corresponding boundary-layer maxima. In figure 8(*b*), which corresponds to case T3Bf, the wall-normal peak in u_{rms} is approximately at $1.3\delta^*$, consistent with the experiments of Matsubara & Alfredsson (2001), whereas in figure 8(*a*), which corresponds to case T3Bs, this peak is at $\simeq 1.65$. The level of u_{rms} above the boundary layer $\delta^* \geqslant 3$ is also significantly higher in case T3Bs. We ascribe these discrepancies to the different levels of boundary-layer contamination at the leading edge, which alter the development of the streamwise Reynolds stress.

In the light of the differences in the development of the Reynolds stresses between cases T3Bs and T3Bf, one may also expect to see significant differences between the respective transition mechanisms. To qualify the differences, we studied the flow fields for these cases visually. The details of this study are presented in § 3.4. An important conclusion that we state here is that, despite the differences in the streamwise Reynolds stress development, cases T3Bs/f undergo transition by the same mechanism.

We close this section with a discussion of the effect of the symmetry condition on cases SLSs/f. Analogous to the T3Bs/f cases, the symmetry condition results in a delayed onset of transition (figure 4). Specifically, transition begins at $x = 110$ ($Re_x = 52\,000$) for case SLSs, in comparison with $x = 60$ ($Re_x = 28\,000$) for case SLSf.

In figure 9(*a*, *b*) we show the profiles of streamwise and wall-normal Reynolds stresses for cases SLSs/f. As observed for cases T3Bf and T3Bs, one sees a sixfold difference between the amplitudes of $\langle vv \rangle$ at $x = 0$. However, the behaviour of the streamwise Reynolds stress in the SLS cases is different from the T3B cases: $\langle uu \rangle$ is higher for case SLSf at all wall-normal locations, and the wall-normal u_{rms} profiles in both cases exhibit a peak at the same location. Figure 27(*a*, *b*) in the online supplement § A.4 shows that this location coresponds to $y = 1.3\delta^*$.

Figures 10(*a*) and 10(*b*) show the evolution of the maximum streamwise Reynolds stress, $\langle uu \rangle$, inside the boundary layer. In figure 10(*b*), the data are normalized using the turbulent kinetic energy at the boundary-layer edge. The agreement between cases SLSs and SLSf up to $x \simeq 30$ in figure 10(*b*) suggests that for the low FST length

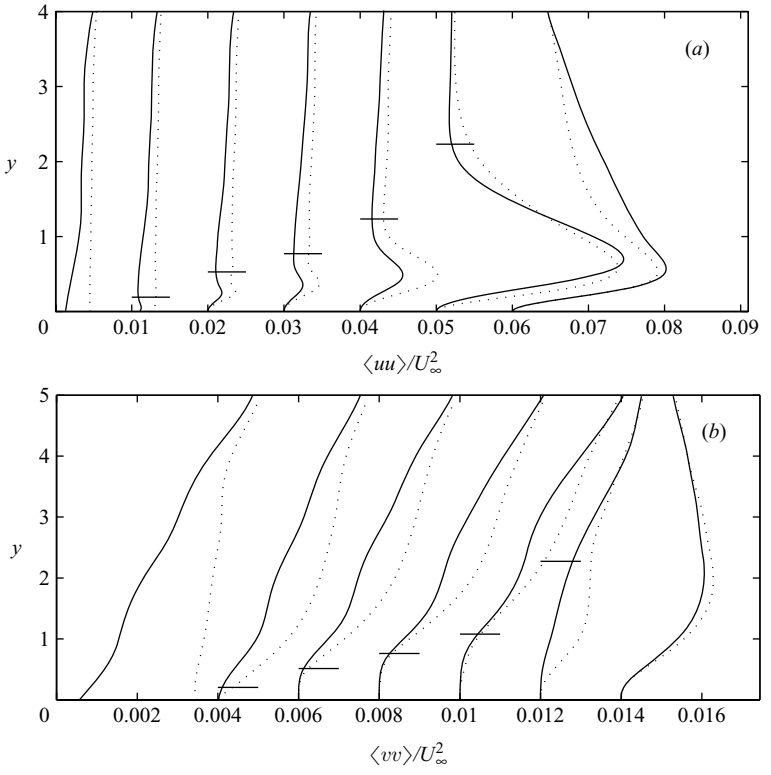

FIGURE 9. Profiles of (a) streamwise Reynolds stress $\langle uu \rangle$, and (b) the wall-normal Reynolds stress $\langle vv \rangle$. From left to right, the plots correspond to $x = 0$, 2, 5, 10, 20, 75, 250; $Re_x = 0$, 940, 2350, 4700, 9400, 35 250, 11 7500. ———, case SLSs; ·····, case SLSf; the short horizontal lines indicate the local boundary-layer thickness δ_{99} On the x-axis, the profiles are offset by 0.01 for (a). In (b) the first two plots are offset by 0.004 for clarity and the rest by 0.002.

scale, $L_{11} = 2.3$, the initial disturbance amplitude is proportional to the turbulence intensity at the boundary-layer edge. Brandt *et al.* (2004) report similar behaviour in their simulations.

Interestingly, figure 10(a) shows that for all cases, rapid increase of the Reynolds stress levels is preceded by a region of slower growth, and that this region has larger extent in the T3B cases. Fransson *et al.* (2005) also observed regions of slower initial growth of u_{rms} before a linear increase. They explained this phenomenon by a 'receptivity distance', i.e. a distance needed for the adjustment of discrepant length scales in the free stream and the boundary layer. Our results are consistent with this possibility, in the sense that the receptivity distance increases with the degree of scale mismatch (e.g. L_{11} vs. δ_{99}), which is greater for case T3B.

From these observations, we conclude that at the lower FST length scale of case SLS, the effect of the symmetry condition was primarily to delay the onset of transition without modifying qualitatively the nature of the Reynolds stress evolution. We may also speculate that the reason for the different behaviour in cases SLS from T3B (i.e. evolution of $\langle uu \rangle$) arises from higher distributed receptivity of the boundary layer to lower-length-scale turbulence. According to this conjecture, the 'deficit' in the streamwise Reynolds stress inside the developing boundary layer caused by the

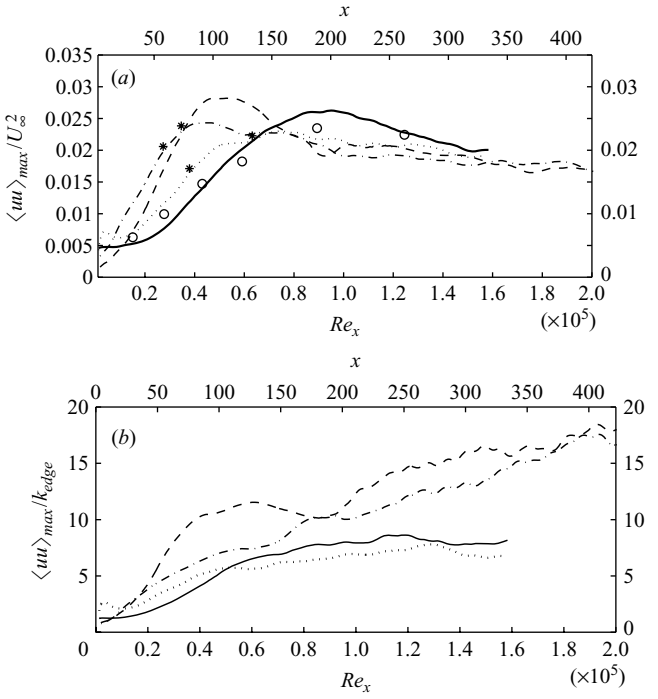

FIGURE 10. Evolution of the maximum streamwise Reynolds stress inside the boundary layer; (*a*) normalized by U_∞; (*b*) normalized by the TKE at the boundary-layer edge: ———, case T3Bs; ·····, case T3Bf; – – –, case SLSs; —·—, Case SLSf; ○, T3B experiment of Roach & Brierley (1992). The asterisks indicate the onset of transitional C_f rise corresponding to $x = 95$, $x = 75$, $x = 100$ and $x = 60$ for cases SLSs, SLSf, T3Bs and T3Bf, respectively.

symmetry plane would be replenished by contamination from the free stream more rapidly in case SLS than T3B. For case T3B, this contamination is retarded by the large disparity between the FST and boundary-layer length scales.

A qualitative comparison of SLSs/f flow fields is made in the online supplement figure 28 (§ A.4), which shows instantaneous contours of the streamwise velocity fluctuation in the (x, z)-plane inside the boundary layer. A higher-amplitude near-wall disturbance environment near the leading edge is seen for case SLSf, and the corresponding boundary layer appears more disturbed throughout the domain, consistent with the more rapid transition onset indicated in figure 4. Aside from the differences in the overall perturbation levels, the two flow fields are very similar. This suggests that the underlying transition mechanism is the same in both instances. At this FST length scale ($L_{11} = 2.3$) and range of FST intensities, transition appears to be accompanied by Klebanoff modes. Their role in transition will be briefly discussed in § 3.4.

3.3. *Two-point correlations*

Two-point spanwise correlations of the velocity signal can provide information on the dominant spanwise length scale of the flow. In transitional and turbulent boundary layers, correlations of the streamwise velocity (u') are used to estimate the average spanwise separation between adjacent streamwise streaks. This distance is taken to be the distance to the first minimum of the correlation function. In figure 11(a, b) the two-point correlation functions of u' are shown for cases SLSs and T3Bs, respectively. The corresponding plots for case SLSf and T3Bf are qualitatively similar. The dashed

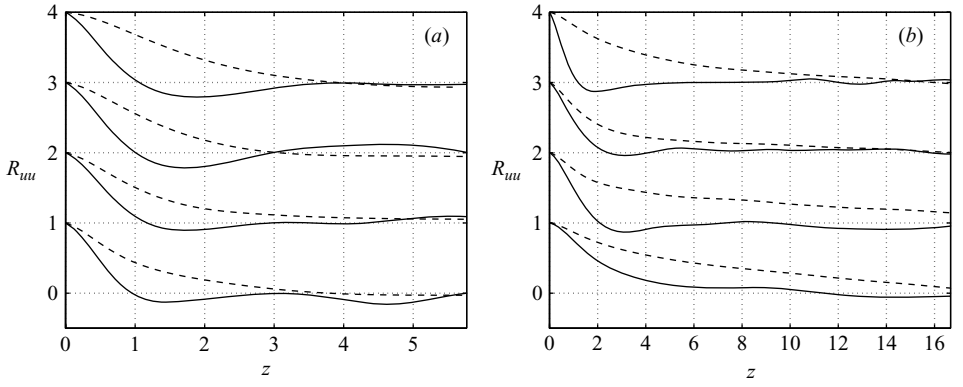

FIGURE 11. Spanwise correlation functions of the streamwise velocity fluctuations; the z-axis is truncated by 50% in each case to focus on the region of significant variation. (a) Case SLSs, R_{uu}; (b) case T3Bs, R_{uu}; ———, correlation functions at the location of maximum boundary-layer u_{rms}; – – –, correlation functions at the boundary-layer edge; from bottom to top: $x = 38$, $Re_x = 19\,000$; $x = 96$, $Re_x = 47\,800$; $x = 154$, $Re_x = 76\,800$; $x = 308$, $Re_x = 153\,600$.

lines represent the correlation function at the boundary-layer edge, and the solid lines the correlation function at the location of maximum u_{rms} inside the boundary layer. The correlation function at the boundary-layer edge indicates a much larger spanwise scale for case T3Bs, as expected. (Note the different ranges of abscissa in figures 11a and 11b.)

The solid curve that corresponds to $x = 96$ ($Re_x = 45\,000$) is located near the onset of skin friction growth for both cases. It can be seen that the spacing between the streaks is approximately 3.4 ($4.1\delta^*$) for the T3Bs case, compared to about 1.8 ($2.8\delta^*$) for case SLSs. The solid curves corresponding to $x = 308$ ($Re_x = 145\,000$) show that in the fully turbulent region, the streak spacing is the same for the two cases, regardless of the differences in the upstream development, indicating a universal turbulent equilibrium. In wall units, defined by $x^+ = xu_\tau/\nu$, where $u_\tau = \sqrt{(1/\nu)\mathrm{d}\langle U\rangle/\mathrm{d}y}$ is the friction velocity, this spacing is 100, consistent with a turbulent boundary layer. These streaks are certainly not the same as their counterparts in the transitional region. Recall from figure 7(a) that the location of the $\langle uu\rangle$ maximum moves close to the wall at the onset of turbulence.

Figure 12(a) shows the streamwise evolution of the location of the minimum of the correlation function. The figure shows that for cases SLSs and SLSf the transitional streak spacing of $\simeq 2$ is established by $x = 75$. For cases T3Bs and T3Bf, the appearance of streaks (with separation $\simeq 3.4$ and 3), is delayed to $x \simeq 100$ and 70, respectively. This was also confirmed by observing the flow field directly. It is interesting to see that while for the T3B cases there is a marked shift in the streak separation distance across the laminar–turbulent transition region, for cases SLSs and SLSf the separation distance does not change significantly. This observation suggests that there is no universal value for streak separation in the perturbed boundary layer. Rather, it may be determined by the FST length scale. Fransson & Alfredsson (2003) performed controlled experiments of boundary-layer transition with and without distributed suction and found that the spanwise streak spacing was virtually unchanged between the two cases, despite a factor 2 reduction in the boundary-layer thickness for the case with suction. They suggested that the scale selection process involves the free-stream length scales. Figure 12(a) shows that

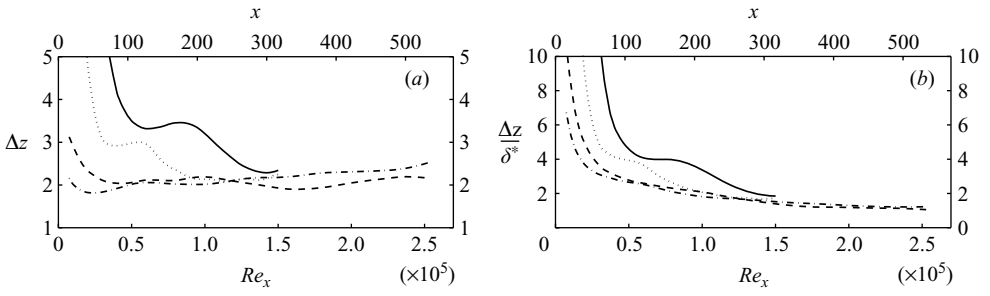

FIGURE 12. Streamwise evolution of the location of the minimum of the spanwise correlation functions of the streamwise velocity; (*a*) in units of R; (*b*) normalized by the boundary-layer displacement thickness; the correlation functions are computed at the location of maximum boundary-layer u_{rms}; ———, case T3B; ·····, case T3B; – – –, case SLSs; —·—, case SLSf.

within the transitional and turbulent regions, the streak spacing slowly increases with the downstream distance. Figure 12(*b*) shows that it slowly decreases relative to the local boundary-layer displacement thickness. Both of these findings are in qualitative agreement with Matsubara & Alfredsson (2001). However, in their experiments, the distance to the correlation function minimum in the transition region tends to $3\delta^*$, whereas our values for cases SLSs and SLSf are closer to $2\delta^*$. For case T3B, the streak spacing is $4\delta^*$ in the transitional region. However, we will show in the next section that the appearance of streaks for this case does not initiate transition.

3.4. *Mechanism of transition in the T3B case*

Jacobs & Durbin (2001) were the first to visualize Klebanoff modes and their breakdown into turbulent spots in a spatial boundary-layer simulation. With the FST intensity set to 3%, the boundary layer developed streaks that were about $1.2\delta_{99}$ apart. Turbulent spot formation was apparently triggered via the penetration of FST into the outer boundary layer. The spots grew in size as they were convected downstream and merged with developed turbulence to maintain its upstream front. Jacobs & Durbin concluded that the low-speed streak provides a path for the direct contamination of the boundary layer with the FST when the streak moves into the outer boundary layer, but is otherwise irrelevant to transition, i.e. no evidence of streak instability was found. The turbulent spots resulting from this FST/boundary-layer interaction were called 'top-down' spots because they originated from an incursion of the FST into the outer boundary layer and spread vertically toward the wall while being convected downstream with the mean flow.

Motivated by previous work on streak instability and breakdown (Andersson *et al.* 2001; Brandt & Henningson 2002), Brandt *et al.* (2004) illustrated a different mechanism. Using planar and three-dimensional images of the flow field, they concluded that in their simulations, the formation of turbulent spots was caused by one of two instability modes of the streamwise streak. The sinuous, or the antisymmetric mode, was observed more often than the varicose, or the symmetric mode. This could be explained by the analysis of Wu & Choudhari (2003) and Andersson *et al.* (2001), who found the sinuous mode to be more unstable.

We note that neither Jacobs & Durbin (2001), nor Brandt *et al.* (2004) observed spots of a well-defined shape. Arrowhead-shaped spots were reported by Matsubara & Alfredsson (2001) in their studies of boundary-layer bypass transition. In this section, we examine the evolution of boundary-layer disturbances for our cases T3Bs

and SLSs using a combination of three- and two-dimensional images. We follow the development of turbulent spots from their birth to their merger with the downstream turbulent front. We note that, because of the high intensity of the background FST, it is difficult to perform a quantitative characterization of turbulent spot precursors, or to compute the leading- and trailing-edge velocities of the spots. We will focus on the T3Bs case since, to our knowledge, the type of FST-induced transition observed in this simulation has not been described before.

The spanwise domain of the T3B simulations is sufficiently large to permit unhindered development of turbulent spots. Four turbulent spots were observed and followed from birth to maturation during the course of the simulation. Two of the spots observed have shapes that point in the streamwise direction, similar to the illustration in figure 4(*b*) in Matsubara & Alfredsson (2001). The other two seem to have rather arbitrary shapes. One spot from each category will be discussed.

Figure 13 illustrates the three-dimensional development of one turbulent spot observed in the T3Bs simulation. The left halves of figures 13(*a*) and 13(*b*) show spanwise-elongated structures at somewhat regular intervals in the streamwise direction. These quasi-periodic structures have a spanwise length of $\simeq 5$, about three times larger than the local boundary-layer thickness $\delta_{99} \simeq 1.6$ (see figure 5*b*). The streamwise separation of adjacent spanwise structures is approximately 7.0, which is five times larger than the local boundary layer thickness, and the period is 12.5, corresponding to a convection speed of approximately 0.56. These structures are stretched in the streamwise and wall-normal directions by the boundary-layer mean shear around $x = 50$ (figure 13*b*), and reorient themselves into a series of horseshoe vortices (these vortices have also been called lambda, Λ-, or hairpin) by $x = 60$ (figure 13*c*, *d*). Birth of additional horseshoe vortices can also been seen to the right of the original trailing horseshoe vortex in this figure. Figure 13(*e*, *f*) shows the same structure at later times, when the horseshoe vortices have increased in number and are organized into a young turbulent spot. At this stage, the shape of this spot is reminiscent of an arrowhead. Two more horseshoe vortices are forming behind and to the right of the spot, suggesting a possible mechanism by which the spot can grow laterally while preserving an arrowhead shape, i.e. by inducing the formation of more vortices on its flanks. Note that streamwise streaks are also present in the figures. In figure 13(*b*), two low-speed streaks (black contours) are seen to the right of the developing horseshoe vortex. However, both of them remain intact in figure 13(*f*), at which point the turbulent spot is mature. Thus, the boundary-layer streaks do not appear to participate in the transition process in the T3B case. Additional, shorter high- and low-speed streaks are also present in figure 13(*d*) around and underneath the growing horseshoe vortices. In this case, the streaks are generated by the horseshoe vortices, and therefore do not initiate the transition process. From figures such as figures 13(*e*) and 13(*f*), we estimated the celerities of the leading and trailing edges of this spot to be 0.88 and 0.72, respectively. The location of the leading horseshoe vortex, and the most downstream location of quiescent flow behind the spot, respectively, were used to compute these values.

3.5. *Origin of the quasi-periodic disturbances*

In figure 14 we show the streamwise evolution of the wall-normal velocity fluctuation along the line $(y, z) = (0.68, 35)$ that passes through the quasi-periodic structures in figure 13. The streamwise structures have the signature of a short wavepacket with the streamwise wavelength λ and velocity c of approximately 7 and 0.6, respectively, corresponding to a period of 12. The wavelength of the wavepacket is defined as the

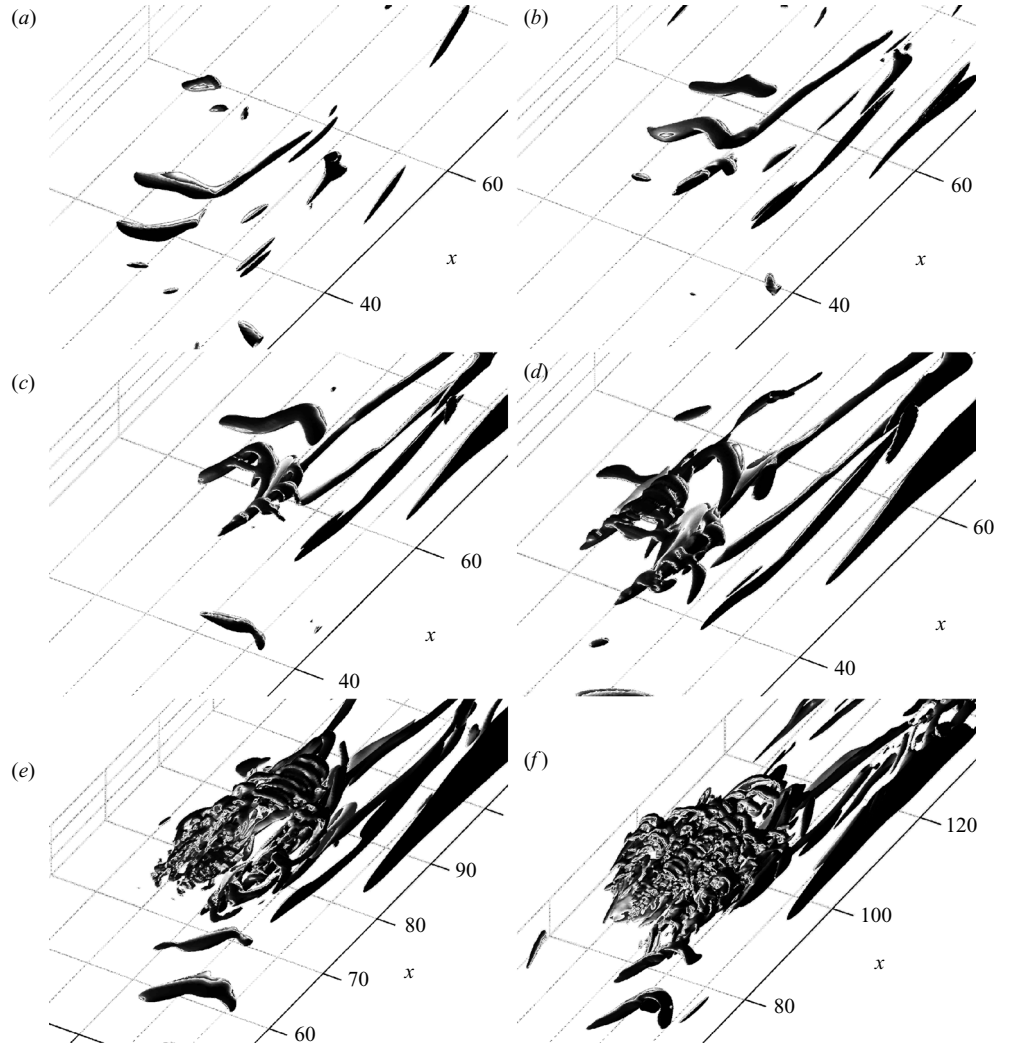

FIGURE 13. Isosurfaces of the streamwise velocity fluctuation, $u' = \pm 0.3$, shown in light grey and black, respectively, and isosurfaces of $Q = 0.015$, shown in dark grey. The images illustrate the development of a turbulent spot from the T3Bs simulation; (*a*) $t = 189$, (*b*) $t = 205$, (*c*) $t = 219$, (*d*) $t = 229$, (*e*) $t = 260$, (*f*) $t = 295$.

average distance between adjacent peaks, and the velocity is computed by dividing the displacement of the most prominent peak in the wavepacket by the coresponding time interval. The approximate local value of $\delta_{99} = 1.2$ yields $\lambda/\delta_{99} = 5.8$. The corresponding frequency ω of the wavepacket is 0.52, which yields for the non-dimensional frequency, $F = \omega\nu/U_\infty^2$, the value 1100.

Nagarajan *et al.* (2007) observed a bypass transition scenario in which boundary-layer disturbances appear in the form of wavepackets in the spanwise velocity signal. The values for the group velocity and wavelength they reported were, on the average, $c = 0.52$ and $\lambda/\delta_{99} = 5$. While these numbers are in approximate agreement with our results, we note that in our case the wavepacket manifests itself in the wall-normal, and not the spanwise velocity component. Thus, the relationship between the transition scenario reported by those authors and the one described here is uncertain.

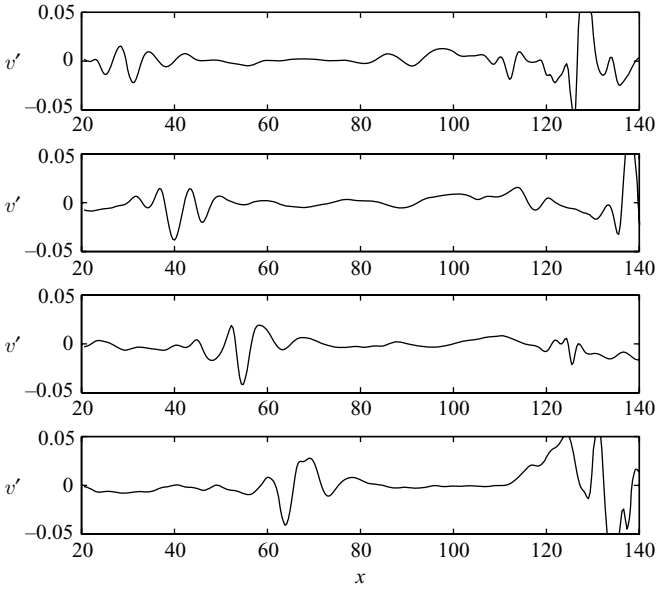

FIGURE 14. Streamwise evolution of the wall-normal velocity fluctuation, v', at location $(y, z) = (0.68, 35)$, showing the movement of a wavepacket. Successive plots are separated by $\Delta t = 16$.

The wavepackets we observe are not due to TS waves. The Reynolds number based on the displacement thickness at the location at which the wavepackets are detected is approximately $Re_{\delta^*} = 250$. The eigenfunctions corresponding to our values of Re_{δ^*} and $F = 1100$ are well within the stability region for a temporally growing wave in a Blasius boundary layer.

Based on their values for c and F, Nagarajan *et al.* also concluded that the wavepackets seen in their simulations are not due to TS waves, for which the corresponding values would be under $c = 0.44$ and $F = 400$ (Jordinson, 1970; Gaster & Grant 1975).

To examine the origins of the wavepackets, in figure 15 we show filled contours of the spanwise vorticity (defined as $\Omega_z = \partial V/\partial x - \partial U/\partial y$) in a plane located at $z = 35$, which cuts approximately through the centre of both wavepackets that are clearly visible in figure 13(*b*). The large contribution by the mean shear, $\partial U/\partial y$, causes high negative values of the vorticity in the boundary layer. The grey scale is adjusted to highlight the increase in the spanwise vorticity during the time period over which the wavepackets are observed. The vector plot superposed on the vorticity contours represents the projection of the velocity fluctuation field onto the plane. Finally, contours of Q are plotted as solid lines at the same value as in figure 13 to indicate the locations of the wavepackets.

Figure 15 shows that the appearance of the wavepackets is associated with regions of high shear that are found inside the boundary layer during the period of wavepacket formation, corresponding approximately to $155 \leqslant t \leqslant 205$, shown in figure 15(*a–d*). These higher levels of shear appear to be caused by large free-stream eddies moving toward the wall and sending high-momentum fluid towards the boundary layer. This is consistent with the velocity fluctuation vectors above the boundary layer in figure 15, $t = 172$, which show that the velocity is directed toward the surface in the vicinity of the shear layer and the wavepacket.

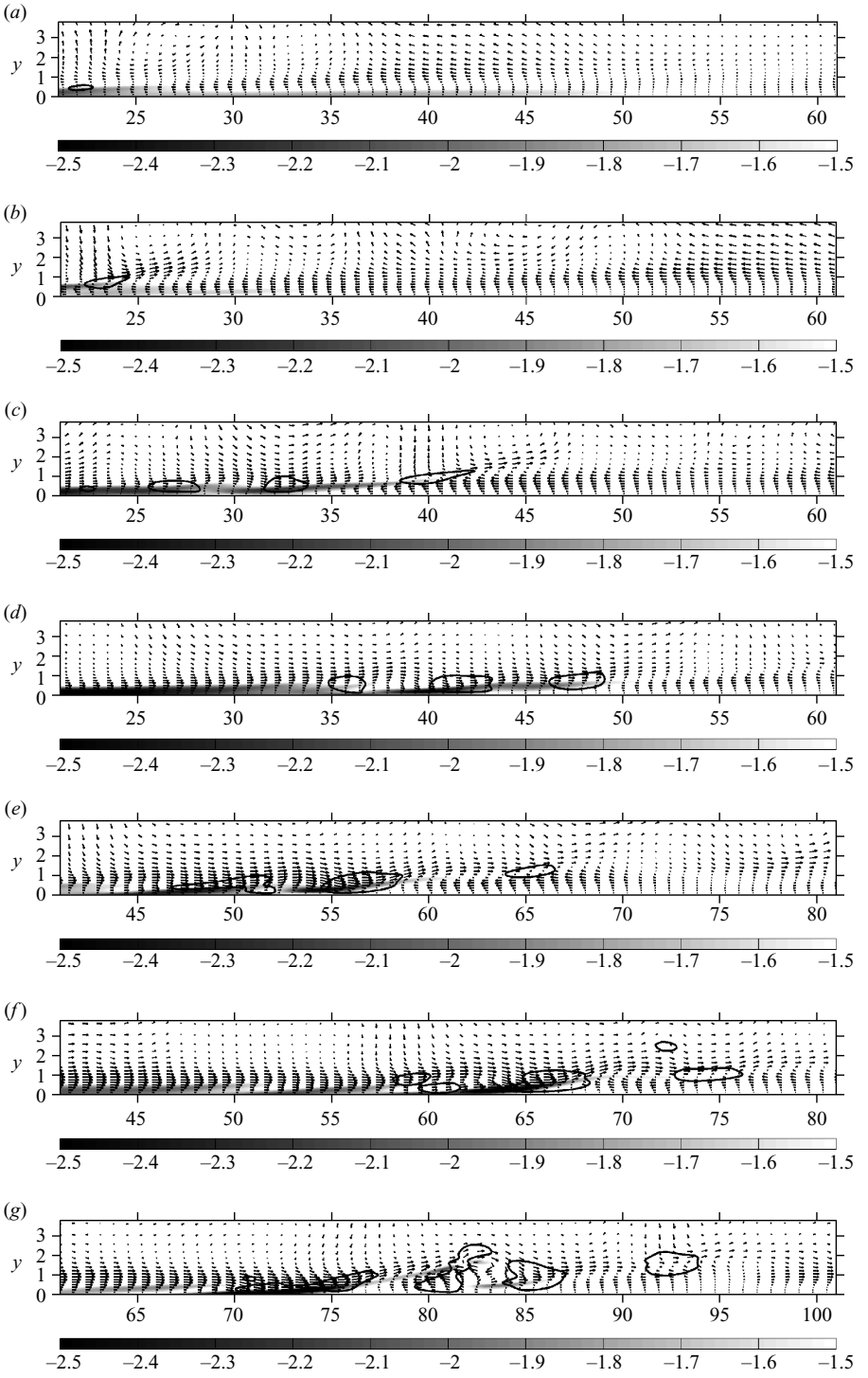

FIGURE 15. Time evolution of a wavepacket in the (x, y)-plane. Filled greyscale contours correspond to the spanwise vorticity, vectors denote the velocity fluctuation, and the thick contours with $Q = 0.015$ highlight the location of the wavepacket. (*a*) $t = 155$, (*b*) $t = 172$, (*c*) $t = 189$, (*d*) $t = 205$, (*e*) $t = 231$, (*f*) $t = 245$, (*g*) $t = 265$.

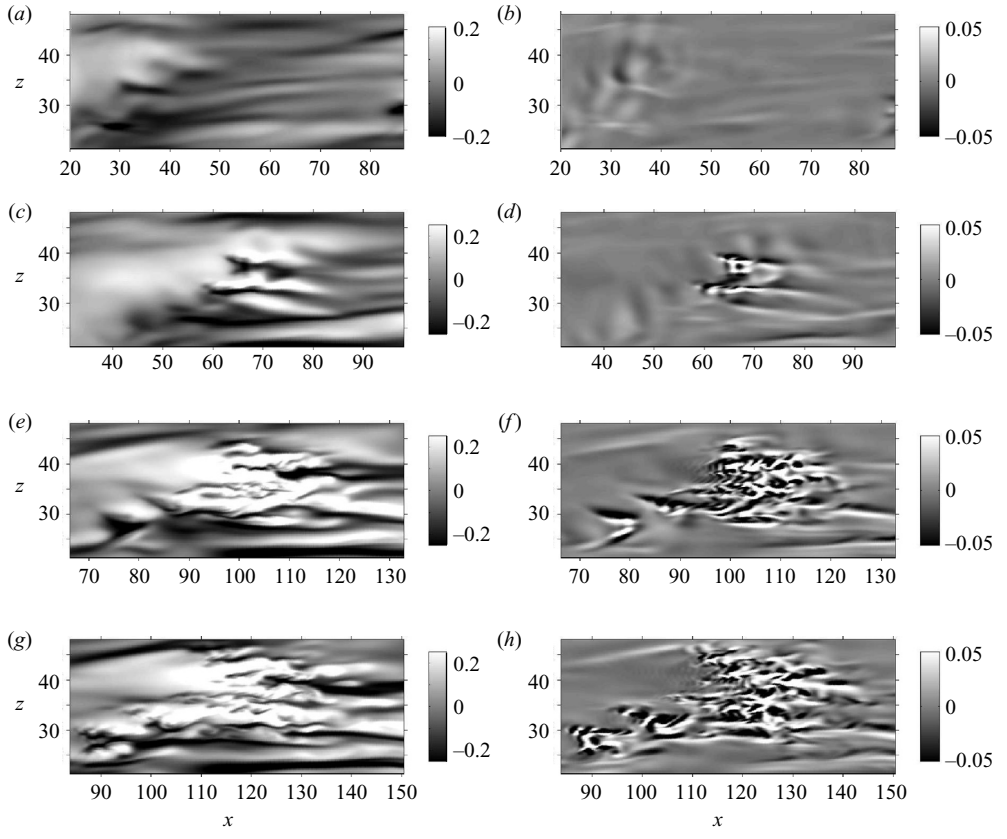

FIGURE 16. Contours of velocity fluctuations for a turbulent spot of type I. Case T3Bs: $y = 0.68$; (*a*), (*c*), (*e*), (*g*) streamwise velocity fluctuation; (*b*), (*d*), (*f*), (*h*) wall-normal velocity fluctuation; (*a*, *b*) $t = 189$; (*c*, *d*) $t = 241$; (*e*, *f*) $t = 296$; (*g*, *h*) $t = 320$.

We can also see from figure 15 that the wavepacket, as identified by the $Q = 0.015$ criterion, occupies a major portion of the boundary-layer thickness. See, for example, figure 15, $t = 189$: the boundary layer thickness δ_{99} is $\simeq 1.2$ at $x = 25$.

3.6. *Further visualizations of turbulent spots*

In this section, we will track the temporal development of two distinct wavepackets into turbulent spots by examining two-dimensional slices parallel to the wall. The spot already shown in figure 13 is termed type I, and the second spot is termed type II.

Figures 16 and 17 correspond to spots of type I and II, respectively, and reveal the features of the spot cross-sections. They complement the three-dimensional images shown in figure 13 and x, y-slices in figure 15.

Again, these figures show no evidence that streak instability is related to the origin of either spot. The spot precursors – the wavepackets – appear as regions of upward- and downward-moving fluid, alternating in the streamwise direction, with small oscillations perpendicular to the direction of the flow. This is shown for the first spot in figure 16(*b*) at $(x, y) = (33, 33)$, and 16(*d*) at $(x, y) = (47, 27)$, where another spot is forming upstream of the main one, and for the second spot in figure 17(*b*) at $(x, y) = (35, 27)$. In the first spot, the ends of the low/high-speed region are then reoriented toward the flow direction, so that the resulting perturbation has the wall-

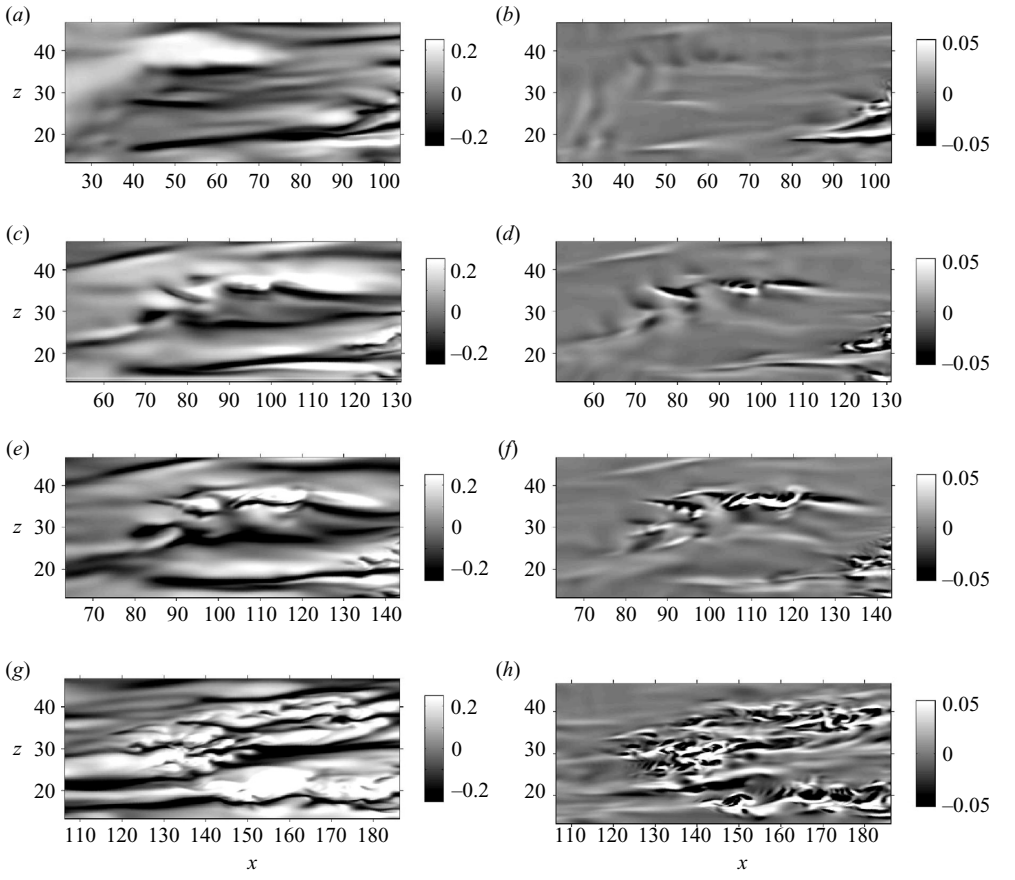

FIGURE 17. Contours of velocity fluctuations for a turbulent spot of type II. Case T3Bs; $y = 0.68$: (*a*), (*c*), (*e*), (*g*) streamwise velocity fluctuation; (*b*), (*d*), (*f*), (*h*) wall-normal velocity fluctuation; (*a*, *b*) $t = 82$; (*c*, *d*) $t = 154$; (*e*, *f*) $t = 179$; (*g*, *h*) $t = 261$.

normal velocity signature of a horseshoe vortex. This is most clearly seen from figure 16(*f*) at $(x, y) = (80, 27)$ in the spot developing upstream. The reorientation of this perturbation is due to the boundary-layer mean shear. When the central part of the low/high-speed region is moved up by the fluctuating velocity, the velocity gradient causes it to move faster than the ends, stretching the disturbance into a $>$ shape. For the second spot (figure 17), only the top half of the low/high-speed region is reoriented toward the streamwise direction, which gives it the appearance of a quasi-streamwise vortex. This is shown in figure 17(*d*) at $(x, y) = (80, 33)$. As a result of the asymmetry, the ensuing turbulent spot does not have a $>$ shape.

Next, the vortical structures develop instabilities, which appear as oscillations in the wall-normal velocity along their axes. These instabilities lead directly to turbulence, in the sense that no coherent structures can be identified once these oscillations are pronounced. This can be seen in figures 16(*f*) at $(x, y) = (87, 32)$ and 17(*f*) at $(x, y) = (93, 35)$. Figure 30 in the online supplement § A.6 shows a magnified view of the upstream horseshoe vortex in figure 16(*e*, *f*) undergoing breakdown to turbulence. A three-dimensional view of the breakdown process can also be seen in figure 13(*a–c*) in the isosurfaces of Q.

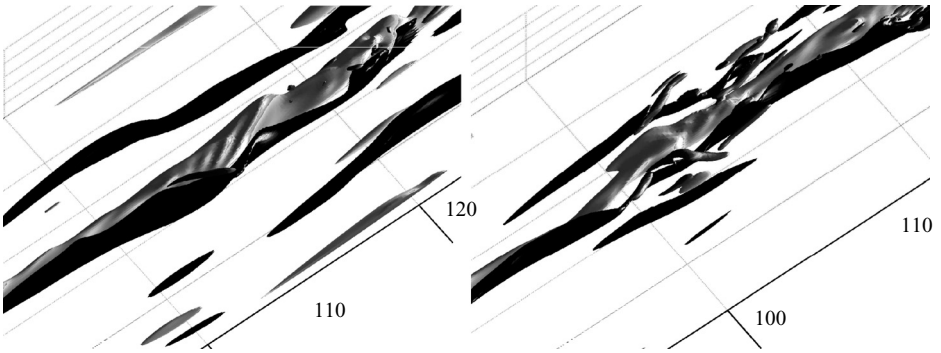

FIGURE 18. Isosurfaces of the streamwise velocity fluctuation, $u' = \pm 0.30$, shown in light grey and black, respectively, and isosurfaces of $Q = -(\partial u_i/\partial x_j)(\partial u_j/\partial x_i) = 0.045$, shown in dark grey. The images illustrate two types of streak breakdown observed for case SLSs; (*a*) $t = 136$; asymmetric breakdown; (*b*) $t = 270$; symmetric breakdown.

The first spot spreads upstream through its lateral edges and merges with the fully turbulent region at $x \simeq 220$. The contours of the wall-normal velocity fluctuation in figures 16(*f*) and 16(*h*) suggest that the shape of the spot points in the streamwise direction. Interestingly, the shape of the second spot appears to be arbitrary up to $t = 261$, at which point it has just merged with another nascent spot developing below it (seen in figure 17(*f*) at $(x, y) = (110, 17)$). The resulting larger spot points upstream (figure 17*h* at $(x, y) = (145, 30)$). This shape persists until the spot merges with the turbulent front (not shown).

Since the Reynolds stresses in the T3Bs case showed a somewhat different development from the T3Bf case in the pre-transitional region, as described in § 3.1, we also examined frame-by-frame the transitional flow field corresponding to the T3Bf case, in which the presence of the full leading edge is expected to result in a more physical flow field. The results of the comparison between cases T3Bs and T3Bf indicate that turbulent spot formation and evolution remain the same. For example, figure 29(*a*, *b*) in the online supplement § A.5 correspond to a young turbulent spot from the T3Bf simulation, and should be compared with figures 16(*e*) and 16(*f*) respectively, which show a turbulent spot in a similar stage of development for case T3Bs.

For comparison with the T3B scenario, we conclude this section with a brief description of breakdown to turbulence for case SLSs. Figure 18 shows three-dimensional images of two streaks undergoing two different types of deformation leading to the formation of turbulent spots. Isosurfaces of positive and negative streamwise velocity fluctuation ($u' = \pm 0.30$) are shown in light grey and black, respectively, and isosurfaces of $Q = -(\partial u_i/\partial x_j)(\partial u_j/\partial x_i) = 0.045$, in dark grey.

The first type of streak deformation is illustrated in figure 18(*a*), which shows two adjacent high- and low-velocity streaks undergoing oscillations about their axes. The second type of deformation observed is shown in figure 18(*b*). The high-speed streak in the middle appears to be undergoing symmetric fluctuations about its axis, as shown by two flanking low-speed streaks (black) and two smaller-scale eddies shown in grey and corresponding to Q isosurfaces. In both cases, breakdown is accompanied by a progressive loss of a well-defined streaky structure and the appearance of smaller-scale eddies, shown by the dark grey contours of Q. Details on the temporal evolution of

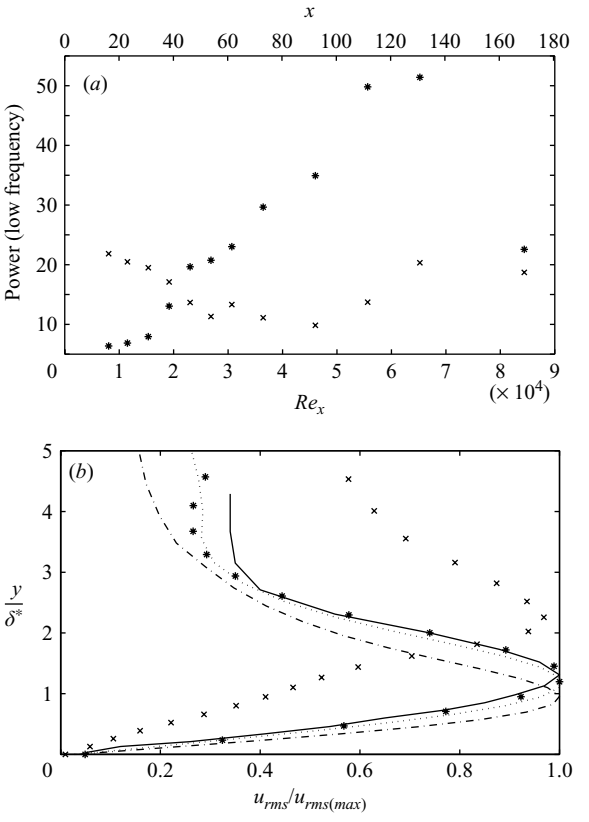

FIGURE 19. (*a*) Evolution of the power in the discrete modes for case SLSs: *, $F \leqslant 15$; ×, $F \geqslant 100$. (*b*) Normalized profiles of u_{rms} across the boundary layer in low-frequency modes (using a sharp Fourier cutoff filter at $F = 10^6 \omega\nu / U_\infty^2 = 15$), except for the curve marked by ×, which represents high-frequency modes ($F \geqslant 100$) at $x = 54$; δ^* is the local displacement thickness; ●, $x = 4$; ·····, $x = 54$; —·—, $x = 73$; ———, data from Matsubara & Alfredsson (2001).

the two streaks including images of the resulting turbulent spots are given in § A.4 of the online supplement.

From our simulations of cases SLSs/f, we cannot determine whether streak breakdown is caused by secondary instabilities. Some support for this conjecture comes from the fact that the two modes of breakdown we observe have asymmetry and symmetry, consistent with the notion of sinuous and symmetric instability. Nevertheless, the background 6% FST in our simulations prevents us from ruling out the scenario proposed by Jacobs & Durbin (2001) in favour of that of Brandt *et al.* (2004).

To underscore the importance of streaks in transition of the SLS cases, we computed frequency spectra of the streamwise velocity at various locations within the computational domains. The wall-normal location at which the spectra are calculated corresponds to the maximum boundary-layer u_{rms}. This position is approximately in the middle of the transitional boundary layer, but moves close to the wall at the onset of turbulence, near $x = 150$. Asterisks in figure 19(*a*) indicate the evolution of energy in the low-frequency portion of the spectrum, $F = 10^6 \omega\nu / U_\infty^2 \leqslant 15$, and figure 19(*b*) shows profiles of the square root of this energy component across the boundary layer.

Comparison of this figure with figure 27 (*a*) from the online supplement § A.4, in which the square root of the total energy (i.e. u_{rms}) has been plotted, suggests that the increase in the boundary-layer u_{rms} for case SLSs is due to energy growth in the low frequencies. For comparison, in figure 19(*a*), we include the evolution of the high-frequency energy component ($F \geqslant 100$). The square root of this energy is also plotted across the boundary layer in figure 19(*b*) for $x = 54$. The corresponding modes are seen to peak closer to the edge of the boundary layer ($\delta_{99} \simeq 3\delta^*$), and, unlike the low-frequency modes, are not amplified in the streamwise direction. These results are consistent with both experiments, e.g. Klebanoff (1971), Matsubara & Alfredsson (2001), and theoretical models (Choudhari 1996; Leib, Wundrow & Goldstein 1999).

An important conclusion from the comparison between transitional flows in the SLS and T3B cases is that, in the former, streamwise streaks actively participate in transition, whereas in case T3B, the transition mechanism is fundamentally different, and involves streamwise wavepackets with spanwise scales much larger than the local boundary-layer thickness.

4. Discussion and conclusion

We have performed four DNS of boundary-layer transition due to 6% FST with the aim of studying the effects of the FST length scale variations on the transition behaviour. Two of the simulations are designed to match the T3B experiment by Roach & Brierley (1992). These simulations are carried out at the FST length scale value of 14, $R_L = 6580$, to match FST evolution in the experiment. This value for the FST length scale is several times larger than typical values ($\simeq 3$) used in previous simulations.

The two simulations (T3Bs/f) differ in terms of the symmetry of the oncoming disturbance field: for case T3Bs, we used a symmetry condition along $y = 0$ in the region upstream of the plate leading edge, and for case T3Bf, the symmetry condition is not imposed, i.e. the full domain is considered. The purpose of the T3Bs case was to permit longer simulation times, and to study the effect of changing the leading-edge disturbance environment on transition.

We performed two additional simulations, SLSs/f, which were almost identical to the T3Bs/f cases, respectively, except for the lower value of the FST length scale. In these two cases, the FST integral length scale is set to 2.3. This value was chosen to match previous simulations, in which transition via the breakdown of Klebanoff modes was reported. The transition mechanism observed for the SLS cases appears the same as reported in previous simulations and experiments, and was compared with the transition mechanism of the T3B case.

The main effect of the symmetry condition on the T3B simulation is a downstream shift in the location of transition. The Reynolds stress development within the boundary layer is altered: the amplitude of the vertical Reynolds stress $\langle vv \rangle$† at the leading edge is reduced by a factor 6 in the T3Bs case compared to the T3Bf case. This discrepancy accounts for different development of the streamwise Reynolds stress downstream of the leading edge. In the T3Bf case, $\langle uu \rangle$ is concentrated in a rapidly growing sharp peak in the middle of the boundary layer, at $y/\delta^* = 1.3$, and in the T3Bs cases it grows more slowly and has a more diffuse wall-normal peak at $y/\delta^* = 1.65$. Noting that at the leading edge, $\langle vv \rangle$ is the component of Reynolds

† At the leading edge, the y-direction is parallel to the vector tangent to the plate tip.

stress that is tangential to the plate surface, we suggested that the sharp $\langle uu \rangle$ peak in the T3Bf cases arises by advection of $\langle vv \rangle$ in the leading-edge vicinity along the curvilinear coordinate of the flat plate. Thus, the boundary layer is receptive to the FST at the leading edge of the plate, i.e. suppression of the $\langle vv \rangle$ amplitude in the vicinity of the leading edge via the use of the symmetry condition results in notable differences in the boundary-layer contamination as measured by $\langle uu \rangle$.

Additional insight comes from comparing cases SLSs/f, which correspond to $L_{11} = 2.3$. The main effect of the symmetry condition is, again, to delay the onset of transition in case SLSs, compared to SLSf. However, although the discrepancy in $\langle vv \rangle$ at the leading edge between cases SLSs and SLSf is similar to that described for the T3B cases, the downstream profiles of $\langle uu \rangle$ inside the boundary layer have the same shape, and exhibit a peak at the same location, $y \simeq 1.3\delta^*$. Furthermore, in the early stages of boundary-layer development ($x = 5$–40), profiles of the maximum streamwise Reynolds stress inside the boundary layer scaled by the TKE at the boundary-layer edge fall on top of each other (cf. figure 10), indicating a 'local similarity', i.e. coupling between the local free stream and the boundary layer. We loosely refer to this coupling as 'distributed receptivity' because the interaction between the boundary layer and the free stream takes place over a finite streamwise region. Thus, for case SLSs, although the attenuated $\langle vv \rangle$ causes a deficit in $\langle uu \rangle$ downstream of the leading edge, this deficit is rapidly replenished through the coupling between the free stream and the boundary layer, in proportion with the overall FST intensity. For this reason, the qualitative development of the perturbed boundary layer is the same in cases SLS. In contrast, the qualitative differences in the behaviour of the streamwise Reynolds stress development observed for the T3Bs/f cases suggest that the distributed receptivity mechanism is weaker, i.e. insufficient to replenish the $\langle uu \rangle$ deficit caused by the attenuated $\langle vv \rangle$ at the leading edge. Finally, we note that the transition delay in the T3Bs is not simply because the $\langle vv \rangle$ is lower along the surface of the plate. In fact, despite significant attenuation near the leading edge, by $x = 5$, the near-wall $\langle vv \rangle$ profiles are essentially identical in the two cases (cf. figure 7). An explanation for the reduced distributed receptivity in the downstream region for cases T3B and SLS may be related to the larger mismatch between the free stream and boundary-layer length scales in the T3B case. For the SLS cases, L_{11} is comparable to the boundary-layer thickness δ_{99} at the onset of transition, and for cases T3Bs and T3Bf, it is approximately six times the transitional δ_{99}. This conjecture is consistent with the fact that, in the limit of large spanwise wavelengths, the transient growth of Klebanoff mode perturbations is known to scale inversely with the spanwise wavelength (Choudhari 1996; Lieb, Wundrow & Goldstein, 1999).

The hypothesis of reduced receptivity does not contradict the conclusion of Brandt *et al.* (2004) and Ovchinnikov *et al.* (2004) that increasing the FST length scale accelerates transition. First, the largest FST length scale used in their simulations was approximately $3\delta_{99}$ at $Re_x \simeq 30\,000$, whereas the FST length scale used in our cases T3B is around $7\delta_{99}$ at this location. Second, these authors used truncated simulations, in which the computation is started downstream of the leading edge at an arbitrarily prescribed Re_x. Therefore, their simulations do not account for the receptivity in the vicinity of the leading edge.

The experiments of Jonáš, Mazur & Uruba (2000), on the other hand, span the range of length scales used in the current simulations, and indicate that increasing the FST length scale moves the transition region upstream. Thus our results are in qualitative disagreement. However, the FST intensity in their experiments was fixed at

3%, compared to 6% in our simulations. It is possible that at the higher intensity, the optimal FST length scale for transition is smaller. Some support for this conjecture comes from the fact that small-scale turbulence penetrates the boundary layer more easily (Brandt *et al.* 2004), but its free-stream intensity also decays more rapidly. Thus, the overall perturbation of the boundary layer is reduced compared to the case of large-scale turbulence, which decays more slowly. Increasing the FST intensity may offset the faster decay of the small-scale turbulence and make it more effective than the larger scales in inducing transition.

The transition mechanism for the SLS cases has been described before (Jacobs & Durbin 2001; Brandt *et al.* 2004) and is different from that in the main simulation cases T3B. The boundary-layer disturbances are low-frequency modes that appear as low- and high-speed streaks of the streamwise velocity. Their energy increases approximately linearly with the streamwise distance after an initial adjustment region, and in the transitional region they have a spanwise separation of $2\delta^*$–$3\delta^*$. The conclusion regarding the involvement of streaks in transition is indirectly supported by the following. The earlier onset of transition in case SLSf relative to SLSs is accompanied by an earlier rise in the streamwise Reynolds stress (figure 10*a*). However, examination of the energy in the u-velocity spectrum shows energy increasing in low-, but not high-frequency modes (cf. figure 19*a*), consistent with known increase in Klebanoff mode amplitude with downstream distance. Furthermore, the wall-normal profile of the low-frequency modes is essentially the same as that based on the full spectrum.

For case T3Bs, we have shown that spot precursors are present as close upstream as $x = 35$, and a small turbulent spot is shown at $x \simeq 65$ (figure 16*c*, *d*). However, streaks with a well-defined spanwise separation first appear around $x \simeq 100$ (cf. figure 12*a*). Thus, these streaks cannot be directly responsible for transition. Their appearance may be unrelated to the turbulent spots, or, alternatively, may be caused by the turbulent spots themselves, since any localized disturbance will be stretched by the boundary-layer mean shear, which will give it a streaky appearance.

The absence of streaks near the leading edge unmasks an alternative transition mechanism. The FST induces a streamwise wavepacket that appears in the wall-normal velocity component. Wavepackets are associated with spanwise vortical structures, which occupy most of the vertical extent of the boundary layer. Unlike the streaks, which are present close to the leading edge in the SLS cases, wavepackets are first detected at $x \simeq 25$ in the T3Bs case. Initially perpendicular to the mean flow, the spanwise vortices subsequently reorient themselves to become partially aligned in the streamwise direction; at this stage, the dominant structures appear either as symmetric horseshoe/lambda/hairpin vortices (two legs) or quasi-streamwise vortices (one leg). The vortices develop instabilities and break down to turbulence. Hairpin vortices appear to generate spots with a shape that points approximately downstream, and single-leg quasi-streamwise vortices lead to spots of arbitrary shape. We note that this mechanism appears different from the one described by Nagarajan *et al.* (2007). First, the disturbance in our case seems to originate from spanwise and not streamwise vorticity, as observed in their work. Second, in our case the wavepackets appear in the wall-normal rather than the spanwise velocity component. Third, in our case, the wavepacket is not confined only to the lower regions of the boundary layer. Fourth, the wavepackets observed by Nagarajan *et al.* (2007) do not develop into turbulent spots of a well-defined shape. One possible explanation for the differences between our results and those of Nagarajan *et al.* is that in their case, the highest Reynolds number based on the FST integral length scale was $Re_L = 2250$, compared

to $Re_L = 6580$ for our cases T3Bs/f. The maximum FST intensity in their simulations is 4.5%, which is also lower than in our simulations.

Hairpin and quasi-streamwise vortices have been found in numerous previous studies of transitional boundary layers. Perry, Lim & Teh (1981) created a turbulent spot by a short pulse of air from a small hole drilled in the floor of their wind tunnel. The spot was composed of an array of 'folds' near the wall, which were similar in appearance to Λ-vortices. It had an arrowhead shape and was trailed by long streaky tails. They hypothesized that a tubulent spot is simply a staggered arrangement of a series of Λ-shaped vortices. Asai & Nishioka (1990) investigated boundary-layer transition at subcritical (i.e. linearly stable) Reynolds numbers, caused by acoustic perturbations near the leading edge. Their smoke visualization study revealed that a hairpin-like structure was important in the transition process. Singer & Joslin (1994) and Singer (1996) performed DNS to study the evolution of a single hairpin vortex in the flat-plate boundary layer and its subsequent development into a turbulent spot. The hairpin vortex was generated by blowing at the wall and its evolution was very similar to that described in previous studies. The spot was composed of hairpin and quasi-streamwise vortices, possessed a clear arrowhead shape and was followed by velocity streaks. In addition, they observed the formation of new hairpin vortices near the trailing edge of the spot.

The similarities between the spots found in our T3B simulations and those observed in the above studies are striking. This might seem surprising since in our case turbulent spots are generated by forcing at the boundary-layer edge and not at the wall. However, the similarity is consistent with the well-established observation that the turbulent spot as described in this and many previous studies is a fundamental feature of transitional boundary layers.

The present results indicate the importance of the FST length scale in determining not only the onset of transition, but also the underlying physical mechanism. Future numerical and experimental studies of boundary-layer transition should consider not only the effects of the Reynolds number based on either the plate thickness or the FST length scale, but also the ratio between the two length scales as an additional parameter. It is possible, for instance, that for a fixed leading-edge geometry, FST of slightly differing length scales will produce different disturbance growth rates inside the boundary layer, which could reconcile the differences in the measured transition onsets among experiments.

V. O. and U. P. acknowledge the financial support of the NASA Langley Research Center under Cooperative Agreement NAG12285. Thanks are also due to Dr Jens Fransson for sharing with us the results of flow visualizations based on wind tunnel experiments at KTH, Stockholm. Finally, we are grateful to an anonymous reviewer for clarification of experimental techniques for measuring Reynolds stress near the wall.

REFERENCES

Andersson, P., Berggren, M. & Henningson, D. S. 1999 Optimal disturbances and bypass transition in boundary layers. *Phys. Fluids* **11**, 134–150.

Andersson, P., Brandt, L., Bottaro, A. & Henningson, D. S. 2001 On the breakdown of boundary layer streaks. *J. Fluid Mech.* **428**, 29–60.

Asai, M. & Nishioka, M. 1990 Development of wall turbulence in Blasius flow. In *Laminar-Turbulent Transition* (ed. D. Arnal & R. Michel), pp. 215–222. Springer.

Balaras, E. 2004 Modeling complex boundaries using an external force field on Cartesian grids in large-eddy simulations. *Comput. Fluids* **33**, 375–404.

Balaras, E., Benocci, C. & Piomelli, U. 1995 Finite difference computations of high Reynolds number flows using the dynamic subgrid-scale model. *Theor. Comput. Fluid Dyn.* **7**, 207–216.

Balaras, E., Piomelli, U. & Wallace, J. M. 2001 Self-similar states in turbulent mixing layers *J. Fluid Mech.* **446**, 1–24.

Blair, M. F. 1983 Influence of free-stream turbulence on turbulent boundary-layer heat transfer and mean profile development. Part I – Experimental data. *Trans. ASME: J. Heat Transfer* **105**, 33–40.

Brandt, L. & Henningson, D. S. 2002 Transition of streamwise streaks in zero-pressure gradient boundary layers. *J. Fluid Mech.* **472**, 229–261.

Brandt, L., Schlatter, P. & Henningson, D. S. 2004 Transition in boundary layers subject to free-stream turbulence. *J. Fluid Mech.* **517**, 167–198.

Chorin, A. J. 1968 Numerical solution of the Navier-Stokes equations. *Math. Comput.* **22**, 742–762.

Choudhari, M. 1996 Boundary-layer receptivity to three-dimensional unsteady Vortical disturbances in free stream *AIAA Paper* 1996-0181.

Collis, S. S. & Lele, S. K. 1996 A computational approach to swept leading-edge receptivity. *AIAA Paper* 96-0180.

Fadlun, E. A., Verzicco, R., Orlandi, P. & Mohd-Yusof, J. 2000 Combined immersed-boundary finite-fifference methods for three-dimensional complex flow simulations. *J. Comput. Phys.* **161**, 35–60.

Fransson, J. H. M. 2004 Leading edge design process using a commercial flow solver. *Exps. Fluids* **37**, 929–932.

Fransson, J. H. M. & Alfredsson, P. H. 2003 On the disturbance growth in an asymptotic suction boundary layer. *J. Fluid Mech.* **482**, 51–90.

Fransson, J. H. M., Matsubara, M. & Alfredsson, P. H. 2005 Transition induced by free-stream turbulence. *J. Fluid Mech.* **527**, 1–25.

Fransson, J. H. M. & Westin, K. J. 2002 Errors in hot-wire X-probe measurements induced by unsteady velocity gradients. *Exps. Fluids* **32**, 413–415.

Gaster, M. & Grant, I. 1975 An experimental investigation of the formation and development of a wavepacket in a laminar boundary layer. *Proc. R. Soc. Lond.* A **347**, 253–269.

Grosch, C. E., Salwen, H. 1978 The continuous spectrum of the Orr-Sommerfeld equation. Part 1. The spectrum and the eigenfunctions *J. Fluid Mech.* **87**, 33–54.

Huai, X., Joslin, R. D. & Piomelli, U. 1997 Large-eddy simulation of transition to turbulence in boundary layers. *Theor. Comput. Fluid Dyn.* **9**, 149–163.

Jacobs, G. J. & Durbin, P. A. 2001 Simulations of bypass transition. *J. Fluid Mech.* **428**, 185–212.

Johnson, M. W. & Ercan, A. H. 1999 A physical model for bypass transition. *Intl J. Heat Fluid Flow* **20**, 95–104.

Jonáš, P., Mazur, O. & Uruba, V. 2000 On the receptivity of the by-pass transition to the length scale of the outer stream turbulence. *Eur. J. Mech.* B/*Fluids* **19**, 707–722.

Jordinson, R. 1970 The flat plate boundary layer. Part 1. Numerical integration of the Orr-Sommerfeld equation. *J. Fluid Mech.* **43**, 801–811.

Kendall, J. M. 1985 Experimental study of disturbances produced in a pre-transitional laminar boundary layer by weak free stream turbulence. *AIAA Paper* 85-1695.

Kim, J. & Moin, P. 1985 Application of a fractional step method to incompressible Navier-Stokes equations. *J. Comput. Phys.* **59**, 308–323.

Klebanoff, P. S. 1971 Effect of freestream turbulence on the laminar boundary layer. *Bull. Am. Phys. Soc.* **10**, 1323.

Klingmann, R. G. B., Boiko, A. V., Westin, K. J., Kozlov, V. V. & Alfredsson, P. H. 1993 Experiments on the stability of Tollmien-Schlighting waves. *Eur. J. Mech.* B/*Fluids* **12**, 493–514.

Leib, S. J., Wundrow, D. W. & Goldstein, M. E. 1999 Effect of free-stream turbulence and other vortical disturbances on a laminar boundary layer. *J. Fluid. Mech.* **380**, 169–203.

Lin, N., Reed, H. L., Saric, W. C. 1992 Effect of leading-edge geometry on boundary layer receptivity to free-stream sound. In *Instability, Receptivity, and Turbulence* (ed. M. Hussaini, A. Kumar & C. Streett), pp. 421–440 Springer.

Luchini, P. 2000 Reynolds-number independent instability of the boundary layer over a flat surface. Part 2. Optimal perturbations. *J. Fluid Mech.* **404**, 289–309.

Matsubara, M. & Alfredsson, H. 2001 Disturbance growth in boundary layers subjected to free-stream turbulence. *J. Fluid. Mech.* **430**, 149–168.

Morinishi, Y., Lund, T. S., Vasilyev, O. V. & Moin, P. 1998 Fully-conservative higher order finite difference schemes for incompressible flow. *J. Comput. Phys.* **143**, 90–124.

Morkovin, M. V. 1969 On the many faces of transition. In *Viscous Drag Reduction* (ed. C. S. Wells), pp. 1–31, Plenum.

Nagarajan, S., Lele, S. K. & Ferziger, J. H. 2007 Leading edge effects in bypass transition. *J. Fluid Mech.* **572**, 471–504.

Orlanski, I. 1976 A simple boundary condition for unbounded hyperbolic flows. *J. Comput. Phys.* **21**, 251–269.

Ovchinnikov, V. O., Piomelli, U. & Choudhari, M. M., 2004 Inflow conditions for numerical simulations of bypass transition *AIAA Paper* 2004-0591.

Ovchinnikov, V. O., Piomelli, U. & Choudhari, M. M. 2006 Numerical simulations of boundary-layer transition induced by a cylinder wake. *J. Fluid Mech.* **547**, 413–441

Perry, A. E., Lim, T. T. & Teh, E. W. 1981 A visual study of turbulent spots. *J. Fluid Mech.* **104**, 387–405.

Piomelli, U., Balaras, E. & Pascarelli, A. 2000 Turbulent structures in accelerating boundary layers. *J. Turbulence* **1** (001), 1–16.

Rai, M. M. & Moin, P. 1993 Direct numerical simulation of transition and turbulence in a spatially evolving boundary layer. *J. Comput. Phys.* **109**, 169–192.

Roach, P. E. 1987 The generation of nearly isotropic turbulence by means of grids. *Intl J. Heat Fluid Flow* **8**, 82–92.

Roach, P. E. & Brierley, D. H. 1992 The influence of a turbulent free-stream on zero pressure gradient transitional boundary layer development part I: test cases T3A and T3B. In *Numerical Simulation of Unsteady Flows and Transition to Turbulence* (ed. O. Pironneau, W. Rodi, I. L. Rhyming, A. M. Savill & T. V. Truong), pp. 319–347. Cambridge University Press.

Rogallo, R. S. 1981 Numerical experiments in homogeneous turbulence. *NASA Tech. Mem.* 81315.

Singer, B. A. 1996 Characteristics of a young turbulent spot. *Phys. Fluids* **8**, 509–521.

Singer, B. A. & Joslin, R. D. 1994 Metamorphosis of a hairpin vortex into a young turbulent spot. *Phys. Fluids* **6**, 3724–3736.

Spalart, P. R 1986 Numerical study of sink flow boundary layers. *J. Fluid Mech.* **172**, 307–328.

Van Dyke, M. 1982 *An Album of Fluid Motion.* The Parabolic Press.

Voke, P. & Yang, Z. 1995 Numerical study of bypass transition. *Phys. Fluids* **7**, 2256–2264.

Wu, X. & Choudhari, M. 2003 Linear and nonlinear instabilities of Blasius boundary layer perturbed by streamwise voritices. Part 2. Intermittent instability induced by long-wavelength Klebanoff modes *J. Fluid. Mech.* **483**, 249–286.

Zaki, T. A. & Durbin, P. A. 2005 Mode interaction and the bypass route to transition. *J. Fluid Mech.* **531**, 85–111.